Experimental and Numerical Analysis of Wind Field Effects on the Dynamic Responses of the 10MW SPIC Floating Wind Turbine Concept

Qun Cao[a,b], Erin E Bachynski-Polić[c,d], Zhen Gao[c,d], Longfei Xiao[a,b,*], Zhengshun Cheng[a,b], Mingyue Liu[a,b]

[a]*State Key Laboratory of Ocean Engineering, Shanghai Jiao Tong University, Shanghai 200240, China*
[b]*SJTU-Sanya Yazhou Bay Institute of Deepsea Science and Technology, Sanya 572024, China*
[c]*Department of Marine Technology, Norwegian University of Science and Technology, Trondheim 7491, Norway*
[d]*NTNU AMOS, Norwegian University of Science and Technology, Trondheim 7491, Norway*

Abstract

Experimental methods are useful to study global responses of floating wind turbines under wind excitations. One experimental technique is based on the regeneration of wind fields in open space in a hydrodynamic laboratory and the use of the performance-matched rotor to produce the equivalent aerodynamic thrust force according to a target wind field. However, for wind generation systems, due to small variations in the output of each fan and differences among the fans, the obtained wind speed varies in space and time, making it difficult to generate the target ideal uniform, constant or time-varying wind fields. For investigating the quality of the wind field in the experiment and their effects on the global responses, numerical simulations under wind only conditions for the full-scale 10MW SPIC wind turbine were compared with the upscaled responses from model tests. Because of the limitation in the generation and measurement of the target wind field, and the model scaling issue for wind turbine aerodynamics considering the TSR variation, there are uncertainties in interpreting the obtained responses. Numerical simulations were then performed to investigate the effects of spatial and temporal variations in wind fields. Wind shear influences 1P and 3P responses. Below the rated wind speed, when the turbulence intensity increases, the average responses decrease and the response spectra are dominated by low-frequency and 3P components. In Kaimal and Mann wind fields with coherent structures, the generated power and pitch motion show fewer fluctuations than in uniform time-varying wind field, while the nonuniform wind field excites greater 1P and 3P responses.

Keywords: Floating wind turbine, Experiment, Numerical simulation, Wind field generation, Spatial and temporal variation, Coherent structure

1. Introduction

Among renewable energy sources, wind energy is believed to be one of the most promising renewable resources, due to its cost-effectiveness, high technological level and low environmental impact [1, 2]. Compared with onshore

---

*Corresponding author
  Email address: xiaolf@sjtu.edu.cn (Longfei Xiao)

wind, some attributes make offshore wind more competitive, such as higher mean wind speed, more powerful electrical output, great area availability, and fewer visual or noise problems, etc [3]. Therefore, wind power is expected to move from land to intermediate and deep waters [4]. Bottom fixed wind turbines become less cost-attractive at a water depth above 40 meters, and floating wind turbines (FWTs) are considered a better alternative [5]. However, the levelized cost of energy (LCOE) of FWTs is still much higher than that of land-based wind turbines because of their higher transportation, installation, repair, and maintenance costs [6, 7]. Some strategies have been adopted to reduce the LCOE of FWTs, such as increasing the power capacity and rotor size and raising the height of the supporting tower [1]. For instance, the DTU 10 MW reference wind turbine [8] developed by Danmarks Tekniske Universitet has been widely studied. In addition, it is necessary to design floating foundations that are suited for the sea state and water depth of specific locations. The sea states and seabed conditions of Chinese seas are significantly different from those of European seas [9]. The continental shelves of China sea have extremely mild slopes [10], which means that the area suitable for floating concept wind turbines only has intermediate water depths [11]. Semi-submersible concept wind turbines are expected to be more competitive in terms of economic feasibility and good hydrodynamic behavior at moderate water depths (40 m-60 m) [12, 13]. However, most of the FWT concepts in existence are limited to operating in deep waters [11]. A semi-submersible FWT concept carrying the DTU 10 MW wind turbine designed by Cao et al. [14, 15], named the SPIC concept, is suitable for China's intermediate water area. This is regarded as the research object in the following investigation.

Unlike oil and gas platforms, the mean offset of the FWT is greatly influenced by the aerodynamic thrust force from the inflow winds [16]. For a wind turbine rotor with a larger swept area, the thrust increases linearly with the rotor area; and for a wind turbine tower with a higher height, the rotor is exposed to a higher wind speed, which also leads to an increasing wind force [17]. As a result of these changes, FWTs are exposed to progressively complex wind field conditions. In previous studies, it was common to use a rather simple constant and uniform wind field model to represent the wind characteristics in experimental studies [18]. Duan et al. [19] investigated the dynamic response of the OC3 spar FWT concept in the Deepwater Offshore Basin, where a 3×3 stacked square fan configuration was utilized to generate a constant and uniform wind field. For a 5 m/s wind velocity case, the turbulence intensity (TI) was generally approximately 20% within the rotor plane. This was induced by the unsteadiness of the wind generation system and had an influence on the wind-induced motions and loads. In the Triple-spar experiment conducted at DHI Denmark [20], the target constant wind was supplied by a 4 m × 4 m open jet wind generator that did not cover the lower part of the rotor swept area. The velocity in this area decreased to approximately 80% of the target value, and the TI reached 10% at the rated speed and reached 20% for the largest wind speed. No quantification of the spatial coherence was made in this model test. In the model tests of a tension leg platform (TLP) FWT in wind-only conditions by Madsen et al. [21], and the wind field generated by the six individual units was measured prior to the basin tests. The lower left corner of the wind field was exposed to low wind speed and high TI, which was caused by a slight nonuniformity of the guiding vanes in the lower left region of the wind generation system. These limitations of wind simulation may show less influence on the small turbines and fixed foundations, but when the wind turbine size becomes increasingly large, the

2

variation of wind in time-scale and space-scale becomes crucial for the dynamic responses of FWTs [22]. Therefore, the effect of wind variation in time and space on the FWT has drawn the attention of researchers. Dolan and Lehn [23] gave an analytical formulation of the generated torque of a three-bladed wind turbine, considering the factor of wind shear. They proved that 3P pulsation could be induced by wind shear. Devinant et al. [24] conducted a wind tunnel test to obtain the aerodynamic properties of an airfoil used on a wind turbine when subjected to incident wind with a turbulence intensity of 0.5–16%. The results revealed that the aerodynamic properties of the airfoil can be significantly influenced by the turbulence level, qualitatively and quantitatively. Lubitz [25] showed that the turbulence intensity increased power production at low wind speeds while reduced power production at high wind speeds. Chamorro et al. [26] carried out a model test to investigate the turbulence effects on a full-scale 2.5 MW horizontal-axis wind turbine and concluded that the turbine power was modulated by turbulence in a complicated way. Li et al. [27] conducted wind channel tests to study how the power characteristics of a horizontal-axis wind turbine reacted to the turbulence intensity and wind shear. Li et al. [28, 18] simulated the power production and global responses of a FWT in a fully turbulent wind field through numerical simulations. Bachynski and Eliassen [29] investigated the global response of spar, semi-submersible and TLP concept wind turbines under the Mann uniform shear model and the Kaimal spectral and exponential coherence model using SIMA software from SINTEF Ocean. The standard deviations of low-frequency responses under operational conditions differ up to 30% to 40% under two different wind field models. In the study of Nybø et al. [22], the Mann model wind field and the Kaimal model wind field were compared with wind fields constructed from offshore measurements and obtained from large-eddy simulations. Although the effects of wind variation at the time-scale and space-scale on the dynamic responses of the FWT have been manifested in some previous studies, some of them were applied to bottom-fixed wind turbines or small-scale wind turbines, which may show differences from the large-scale 10 MW FWT system. The wind field show characteristics in time-scale (turbulence intensity) and space-scale (wind shear and coherent structure). The above three factors were always studied together in previous studies, but their individual effects should be investigated extensively.

This study aimed to investigate the wind field effect through experimental and numerical methods. A fully coupled aero-hydro-servo-elastic numerical model of the 10 MW SPIC floating wind turbine concept was established, and numerical simulations were performed for the full-scale model, which were then compared with the upscaled dynamic responses from the model test in Section 5. A series of constant or time-varying winds were simulated in the model test, while it was not possible to generate the ideal target wind fields due to the limitations of the experimental facilities. In numerical simulation, it is inaccurate to only simulate the theoretical wind field, which will lead to inconsistency between the numerical and experimental external environmental conditions. The measured wind speed time history at multiple designated points was input into the numerical software, for reproducing the measured wind field as realistically as possible. The numerical wind field conditions which best reflects the simulated wind field in the model test were used to validate the numerical models. The difference between the numerical and experimental results could show the effects of spatial and temporal variations in the wind field. However, due to the limitation of the wind generation system in the model test, the details of such spatial and temporal wind field effects could not be studied

3

experimentally. Therefore, in Section 6, a numerical sensitivity analysis was performed to study how different responses such wind fields will cause. Four kinds of rated-speed wind fields with respect to temporal and spatial variations of the wind speed, namely "uniform and constant", "shear and constant", "uniform and spectral", and "turbulent" were established to investigate the impact of wind shear, turbulence intensity and coherent structure of the wind fields. Moreover, the numerical and experimental comparison in Section 5 used the operation mode, which maintained the rotor speed and blade pitch angle at fixed values corresponding to the mean wind speed, as done in the model test. When studying the dynamic behavior of the FWT under realistic conditions in Section 6, the active rotor controller and blade pitch controller were used to give real-time feed back to regulate the aerodynamic force. The effects of these different operation modes were also studied in this research.

2. SPIC concept description

In this study, a 10 MW semi-submersible FWT concept, named SPIC [15], proposed for the characteristics of China's seas, was regarded as the research object. This FWT system consists of the DTU 10 MW reference wind turbine [8], a redesigned tower, and a semi-submersible foundation with a simple structure. Its side columns are partially inclined outwards, which can significantly improve the stability of the FWT and make it suitable for intermediate water depths. The configuration of the SPIC concept floating wind turbine, as seen in Fig. 1 (a), has been illustrated in Cao et al. [30], and the main parameters of the FWT system are listed in Table 1. The mooring system proposed in this concept is shown in Fig. 1 (b). It is a hybrid mooring system consisting of clump weights and catenary lines, and the parameters are listed in Table 2.
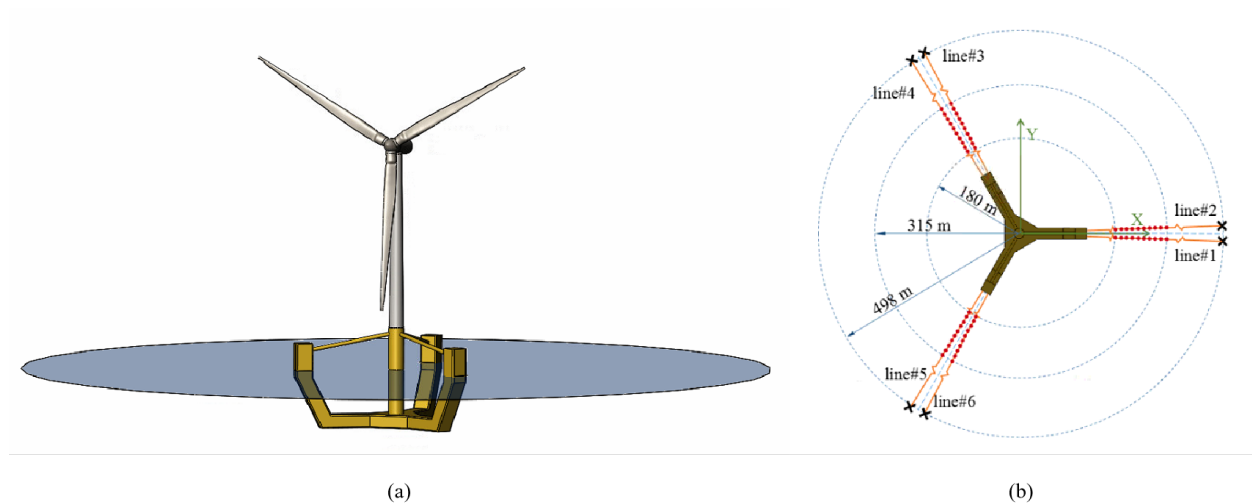

Figure 1: The configurations of (a) SPIC concept FWT and (b) mooring system (red markers indicate clump weights).

4

Table 1: The dimensions and main parameters of the FWT system.

Parameter	Value& Unit
Rated power	10 MW
Cut-in, rated, cut-out wind speed	4.0 m/s, 11.4 m/s, 25.0 m/s
Minimum and maximum rotor speed	6.0 rpm, 9.6 rpm
Gearbox ratio	50
Rotor diameter	178.3 m
Hub height above water line	119.0 m
Height of central column and pontoons	46.0 m, 7.0m
Height of upper and lower side columns	18.0 m, 20.0 m
Diameter of central column	8.3 m
Side length of side columns and pontoons	9.0 m, 9.0 m
Distance between central and upper side columns	50.0 m
Draft	30.0 m
Water depth	60.0 m
Waterplane area	297.10 m^2
Displacement	1.64 E7 kg
Metacentric height	10.85 m
Center of gravity below MWL (CoG)	9.79 m

Table 2: Properties of the hybrid mooring system.

Parameter	Full-scale	Model-scale
Number of mooring lines	6	6
Angle between each group of lines	120 deg	120 deg
Angle between adjacent lines	5 deg	5 deg
Fairlead above MWL	15 m	0.234 m
Anchor below MWL	60 m	0.938 m
Radius from platform center to fairleads	54.5 m	0.852 m
Radius from platform center to anchors	498.0 m	7.781 m
Length of mooring line	465.0 m	7.266 m
Outer diameter of mooring line	0.095 m	-
Mass of mooring line in water	0.190 t/m	0.045 kg/m
EA of mooring line	7.788E5 kN	2.898 kN
The number of clumps on each line	10	10
Each clump weight in air	3.8 t	0.014 kg
Clump position from fairlead	180 m-15 m-315 m	2.813 m-0.234 m-4.922 m
Pretension	478.2 kN	1.780 N
Minimum breaking strength	7325 kN	-

3. Experimental method and calibration test

Experimental methods were used to explore the effects of different wind fields on the performance and dynamic responses of the SPIC concept FWT. The model tests were conducted in the Deepwater Offshore Basin at Shanghai Jiao Tong University, as shown in Fig. 2. All of the experimental cases were carried out with a geometrical scaling ratio of 1:64 and a basin water depth of 0.94 m (corresponding to 60 meters at full-scale). A wind generation system was installed in the basin to meet the target wind conditions. In this section, the simulation of the wind field at the model scale and the model scaling method of each part of the floating wind turbine system are briefly introduced, and the detailed introduction may be found in Cao et al. [30]. The forces and motions responses of the FWT system were obtained through a variety of sensors. The measured responses including the forces on the tower-top and tower-base, the accelerations of the nacelle, and the 6DOF motions of the platform. All of these responses follow the coordinate system shown in Fig. 3. The accuracy of the load measurements can be proved through the strict check of the six-component force sensor. Taking the x-direction shear force as an example, the calibrated relationship between mass and voltage is given in Fig. 4. Then, some known masses were applied to check the accuracy of the measurement. The measured masses are shown in Fig. 4 and the relative errors are also given.
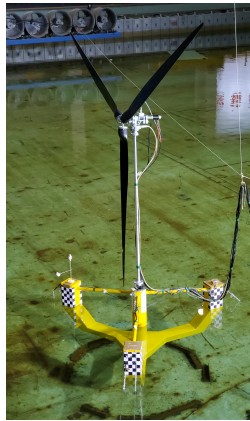

Figure 2: Model-scale 10 MW SPIC wind turbine in the offshore basin.

Before carrying out the experimental and numerical tests of the SPIC concept in complex environmental cases, calibration tests of the wind generation system and FWT models were required, to ensure that the dynamic response characteristics could be captured properly and accurately.

3.1. Wind generation system

A purpose-built wind generation system composed of twenty variable-frequency axial flow fans was adopted in the model test, as shown in Fig. 5. The twenty axial flow fans are distributed in four rows and five columns, and the system has an effective wind area of 4.0 m × 3.2 m. It can control the generated wind speed in real time by adjusting the rotational speed of individual axial flow fans, realizing a wind speed variation range of 0-8 m/s. To increase
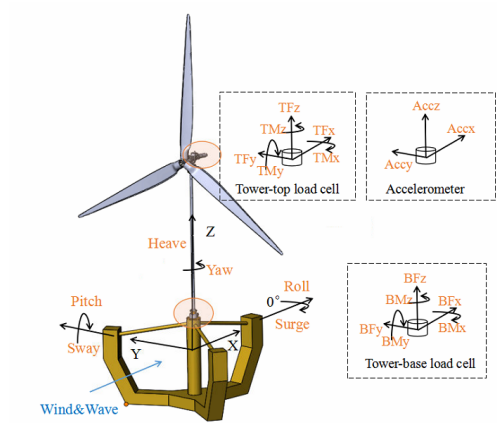
7

Figure 3: Definition of the global coordinate system and the 6DOF motions of the FWT system. The local coordinate systems of tower-top and tower-base loads are also defined.
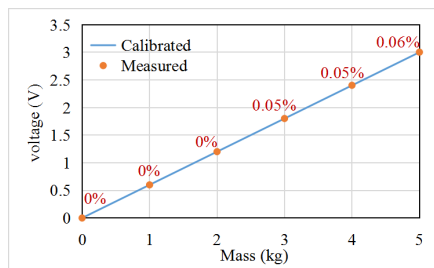

Figure 4: The calibrated and measured relationship between mass and voltage for x-direction load measurement (The percentage data in red color indicate the errors between calibrated and measured values).

the uniformity of the wind field, a honeycomb network was installed in front of the wind generation system. The rotational speed of each axial flow fan can be tuned together or individually. Constant and uniform wind fields can be approximated by setting the rotational speed of all twenty axial flow fans as a constant value. In addition, this wind generation system can be utilized to generate time-varying wind according to a certain wind spectrum. The rotational speed of the axial flow fan at each moment can be deduced according to the theoretical wind speed time history. Therefore, time-varying wind can be generated by giving a rotational speed change command to the wind generation system. It must be noted that the generated wind field does not perfectly match all the target wind fields, due to due to small variations among the fans and small variations in the output of each fan. Therefore, prior to the basin model test, the generated wind fields were checked and recorded on land, to obtain reliable wind speed measurements.
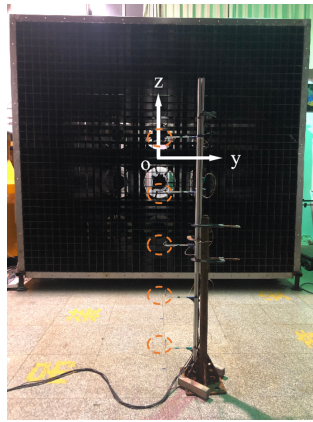
Figure 5: Configuration of the wind generation system and the hot-wire anemometers (circled by orange dotted lines).

3.1.1. Method for wind field calibration

The multi-channel hot-wire anemometer (HWA) was utilized to measure the wind speed. Before the wind field calibration, it is necessary to evaluate the accuracy of the HWA. During the calibration test, we used one probe to measure the wind speed at a certain point in the wind field 20 times. The sampling frequency was set to 100 Hz and the sampling time was three minutes. The mean values and turbulence intensities of these 20 tests are listed in Table 3, and then the random uncertainty can be evaluated through[31]:

$$U = \frac{s(x_i)}{\sqrt{n-1}}, \tag{1}$$

where $s(x_i)$ is the standard deviation of n repeated tests. The random error of mean wind speed is 0.001 m/s, and the random error of turbulence intensity is 0.024%. The systematic error has not been assessed.

A total of five probes were used to measure the wind field at the same time, so each measurement could obtain the wind speed time histories at five different points. The five probes, circled by orange dotted lines in Fig. 5, were installed on a movable device. By moving this device, the wind speed in x-direction at different locations in the wind field can be measured. The sampling frequency was set to 100 Hz and the sampling time was three minutes. The origin

9

Table 3: The mean values and turbulence intensities of wind speeds in 20 repeated tests.

Random	R1	R2	R3	R4	R5	R6	R7	R8	R9	R10
Mean (m/s)	1.405	1.414	1.411	1.408	1.408	1.411	1.411	1.412	1.412	1.408
TI (%)	3.280	3.175	3.236	3.107	2.917	3.140	3.021	2.995	3.015	3.006
Random	R11	R12	R13	R14	R15	R16	R17	R18	R19	R20
Mean (m/s)	1.406	1.410	1.409	1.410	1.409	1.402	1.412	1.410	1.409	1.408
TI (%)	2.997	3.075	2.998	3.121	3.097	2.824	3.094	3.098	2.976	3.053

of the coordinate system (o-xyz) of the wind field is at the center of the wind generation system. The positive direction of the x-axis is along the wind inflow, and the positive directions of the y-axis and z-axis are defined in Fig. 5. Because the rated wind speed of 11.4 m/s is an essential value, the corresponding model-scale wind speed of 1.4 m/s was used as the targeted wind speed to check the quality of the wind field.

It was necessary to determine the proper location of the wind turbine model. First, to determine the location of the wind turbine model in the x-direction, the wind speed was measured at some points in the xoz plane. A group of measuring points was set every 0.5 m, from 0 m to 5.5 m. Each group of measuring points contained 9 position points. The wind speeds at these points were measured by moving the anemometer device several times. Therefore, the obtained results at different locations were not measured at the same time. The model-scale mean wind speeds and turbulence intensities in the xoz plane are shown in Fig. 6. The x-axis represents the distance relative to the outlet of the wind generation system, and the red dashed lines represent the boundary of the area covered by the rotor. It can be seen in the figure that the wind speed distribution was not uniform in the area close to the wind generation system. The average wind speed at each measurement point in the region within the range of 4 m-5.5 m from the wind generation system was basically equal to the target value of 1.4 m/s. This part of the area had relatively good uniformity and could be selected as the longitudinal position for the wind turbine model. On this basis, combined with factors such as the load-bearing structure at the basin bottom and the position of the mooring system in the basin model test, x=5.2 m was determined to be the most suitable distance.

When the longitudinal position was determined, the wind field quality in the yoz plane corresponding to x=5.2 m was checked. The target wind speed of 1.4 m/s was also taken as an example. Eight-one (9×9) measuring points were evenly distributed in a square wind field with a side length of 3.2 m. When measuring, it was necessary to move the anemometer device several times to measure the wind speed on this plane. The model-scale mean wind speeds and turbulence intensities in the yoz plane are shown in Fig. 7. The red dashed circle represents the outline of the wind turbine rotor. In the rotor area, the mean wind speed and turbulence intensity at each measurement point were similar, which means that the uniformity of this plane was acceptable.
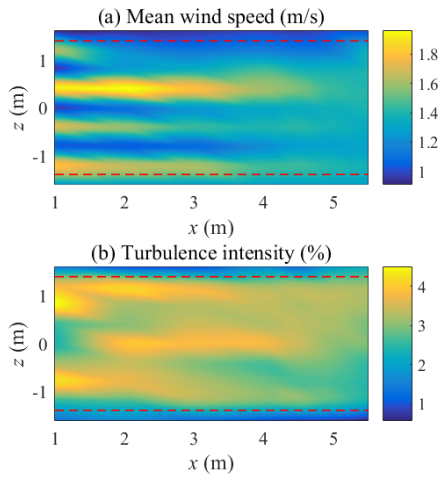
10

Figure 6: The model-scale (a) mean wind speeds and (b) turbulence intensities in the xoz plane. (Target wind speed is 1.4 m/s and target TI is 0%.)
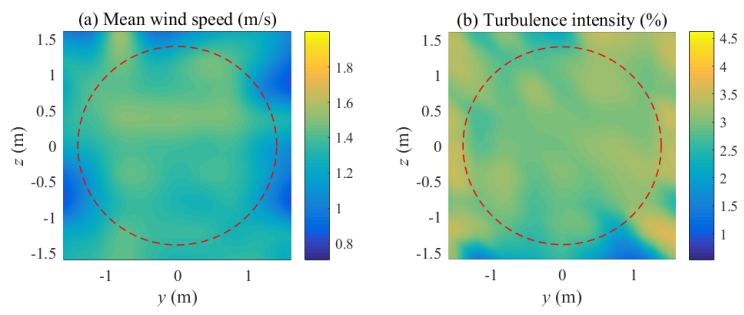

Figure 7: The model-scale (a) mean wind speeds and (b) turbulence intensities in the rotor plane. (Target wind speed is 1.4 m/s and target TI is 0%.)

11

159   After checking the spatial uniformity of the plane where the rotor model was located, it was necessary to guarantee

160 that the generated wind reached the target wind speed as accurately as possible at the selected plane. Therefore, the

161 next step was to obtain the corresponding relationship between the wind speed in rotor plane *Um* and the rotational

162 speed *n* of each axial flow fan. One of the five probes was placed at the center of the rotor plane, and four other probes

163 were set around it. When the wind generation system was given different rotation speeds from 0 rpm to 1600 rpm, the

164 wind speeds measured by these five probes were recorded. Taking the average of the measurement results of the five

165 probes, the corresponding relationship can be obtained in Fig. 8. The corresponding relationship was linear, so the

166 wind speed at the selected plane could be controlled by tuning the rotational speed of the wind generation system.
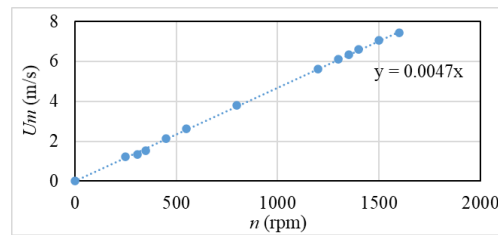

Figure 8: Corresponding relationship between wind speed and the rotational speed of axial flow wind generation system.

167 *3.1.2. Accuracy of generated wind field*

168   When the corresponding relationship between wind speed and the rotational speed of the axial flow wind generation

169 system was obtained, the wind conditions used in this study could be simulated and checked. This study focused on

170 a series of wind-only tests in Table 4. Rated wind speed conditions, below-rated wind condition, over-rated wind

171 condition, and over cut-out wind condition were all taken into consideration. Wind fields in EC1-EC4 were all intended

172 to be constant and uniform. Two rated wind conditions EC5-EC6 with target turbulence intensities (TIs) of 10.0% and

173 14.6% were added to investigate the effect of temporal turbulence of wind. These tests were designed to have spatial

174 uniformity. Due to the limitations of the model test, it was not possible to measure the wind speed time history of

175 each spatial point in the wind field during the basin test under each environmental condition. Therefore, only the wind

176 speeds at the position of hub center were measured and recorded under all six environmental conditions.

177   For conditions with constant wind speeds, such as EC1-EC4, it was only necessary to set the corresponding constant

178 rotational speed for the wind generation system. The time series of these four wind speeds at the position of hub

179 center are measured and recorded. The calculated mean values and turbulence intensities are listed in Table 4. The

180 "constant wind" generated in the model test showed accurate mean values. Only for rated condition EC1, the wind

181 speed time history of 81 points in yoz plane were recorded in the calibration process. These measured values could

182 give more direct results of the time-scale speed variation and space-scale speed coherency. In principle, all the 81

183 measurement points can be used for the analysis of coherence. Here, nine points were selected on the hub point and

184 positive y axis and z axis, as shown in Fig. 9 (a), to illustrate the wind spectra and coherence. The point at hub center

185 was seemed as a reference point, and the points on the vertical and lateral directions with the distance of 25 m, 50 m,

Table 4: Full-scale target and measured wind under six environmental conditions.

| Target wind type	EC	Wind speed	Rotor rotational speed (1P)	Target mean speed & TI	Measured mean speed & TI
Constant and uniform	EC1	Rated	1.0 rad/s	11.4 m/s & 0.0%	11.2 m/s & 3.1%
	EC2	Below-rated	0.76 rad/s	9.0 m/s & 0.0%	9.2 m/s & 2.3%
	EC3	Over-rated	1.0 rad/s	14.0 m/s & 0.0%	14.1 m/s & 3.3%
	EC4	Over cut-out	1.0 rad/s	30.0 m/s & 0.0%	28.8 m/s & 5.2%
Time-varying and uniform	EC5	Rated	1.0 rad/s	11.4 m/s & 10.0%	11.5 m/s & 10.7%
	EC6	Rated	1.0 rad/s	11.4 m/s & 14.6%	11.6 m/s & 14.9%
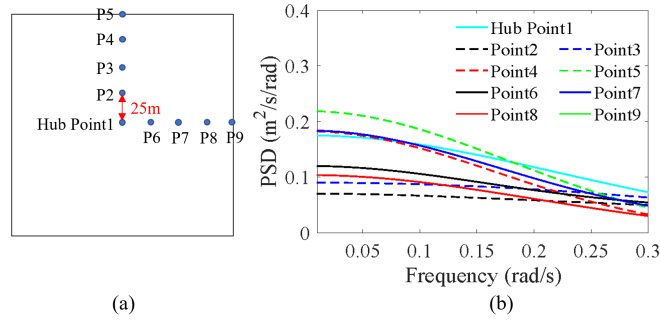
Figure 9: (a) The position of nine selected points in the wind field; (b) Wind spectra of the nine selected points under EC1 (in full-scale).

75 m and 100 m were also selected. The wind spectra of all of nine selected points are shown in Fig. 9 (b). Power can be seen at low-frequency range. The component in wind spectra looks like a white noise, and does not follow a specific spectrum type. During the rotation of the axial flow fan, the wind speed generated at each moment is not exactly the same. Therefore, there will be a little unavoidable turbulence for the "constant" wind conditions. The co-coherence and quad-coherence as functions of frequency, as shown in Fig. 10, was used to visualize the coherence between the reference point and the point with the given distance in the measured wind field. The definitions of co-coherence and quad-coherence are interpreted in Section 4.2.1. The co-coherence in the lateral direction is generally better than the coherence in the vertical direction. The co-coherence values are all between 0.7 and 1, which means the wind field generated by the wind generation system is relatively uniform. The quad-coherence values are all close to zero. The magnitude of the quad-coherence is fairly small for the across-flow separations, compared to the co-coherence. Fig. 9 and Fig. 10 reflect the temporal and spatial characteristics of the wind field presented in Fig. 7 in a more detailed and quantitative manner. The overall quality of the wind generation for constant wind is acceptable, but not perfect.
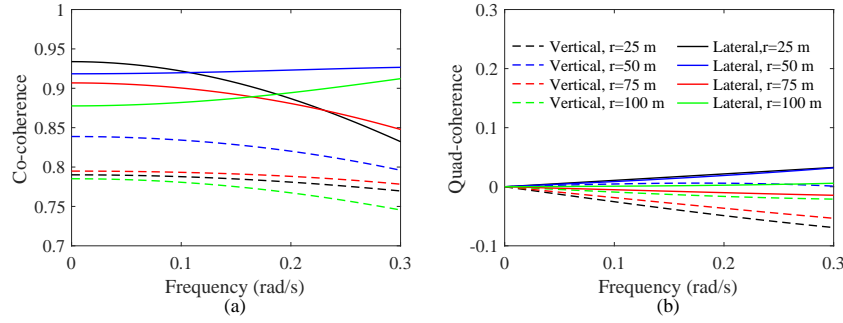
13

Figure 10: (a) Co-coherence and (b) quad-coherence between the hub point and the point with the given distance under EC1 (in full-scale).
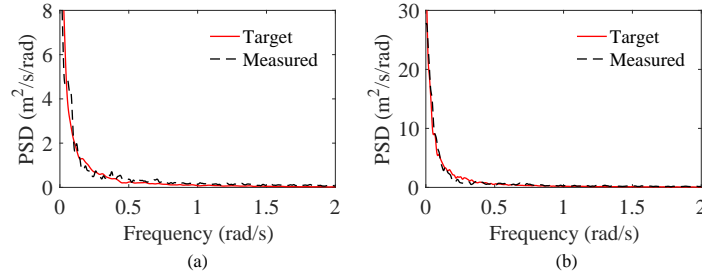

Figure 11: Targeted and measured wind spectra of two time-varying winds in (a) EC5 and (b) EC6 in full-scale.

In addition, time-varying winds in EC5 and EC6 generated by the wind generation system were measured before the model tests to check whether they follow the target IEC spectra. According to the calibration curve in Fig. 8, the rotational speed of the axial flow fan at each moment can be deduced according to the theoretical wind speed time history. Therefore, time-varying wind can be generated by giving a rotational speed change command to the wind generation system. The mean measured wind speeds of EC5 and EC6 are both approximately 11.4 m/s and the turbulence intensities are simulated close to the target values. Fig. 11 shows the wind spectra of two time-varying winds in EC5 and EC6. The low-frequency wind component increases with increasing turbulence intensity. The wind spectra were simulated correctly and accurately. To eliminate the interference of environmental factors as much as possible, it is necessary to ensure that the time history data of wind speed used in the numerical simulation are the same as those used in the experiment. Therefore, the wind speed data at hub center recorded during the calibration tests are input into the numerical simulation.

3.2. Rotor model

The rotor model, consisting of blade models and control system, decides the main aerodynamic forces acting on the FWT model. The Reynolds numbers of the model-scale blades decrease significantly compared with that of the prototype. However, when the Reynolds numbers are at this magnitude, the flow is still turbulent. To achieve

14

213 the targeted thrust and realistically simulate the aerodynamic performance of the wind turbine through experiments,

214 thrust-matched blades [32] were used instead of geometry-matched blades. In this way, the model-scale blade at a low

215 Re number can reach the target thrust of the prototype-scale blade under a high Re number. The C_t coefficients of the

216 full-scale blade (modeled in FAST) and the performance-matched blade (in the model tests) are compared in Fig. 12.

217 This comparison is for a fixed foundation, neglecting floater motions. When the mean wind speed is 11.4 m/s, the

218 TSR=7.86. For the time-varying wind, the rotor speed ω and the blade pitch angles are always set to constant values.

219 Therefore, the TSR (= $\omega R/V$), which is only influenced by inflow wind speed, varies from 6.89 to 8.96. When this

220 performance-matched blade was designed, C_t is basically satisfactory between this TSR range.
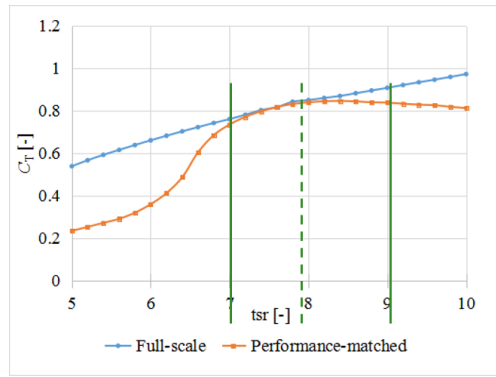

Figure 12: C_t coefficients of the full-scale blade used in FAST and the performance-matched blade used in the model test.

221 A motor was installed inside the nacelle and there were three blade pitch angle adjusting devices. The motor

222 installed in the nacelle can control the rotor to rotate at any speed, and the rotor speed can be fed back and monitored

223 during the model test. There was an angle index on each blade root. The pitch angle of each blade can be manually

224 adjusted before each model test according to the different working conditions. However, the blade pitch angle could

225 not be varied actively during the model test. For example, if the mean wind speed was set as the rated wind speed,

226 regardless of whether the relative wind speed was below, at or over 11.4 m/s, the rotor speed was maintained at 9.6 rpm,

227 and the blade pitch angle was always 0 deg. To summarize, in the model test, the control system no longer converts

228 wind energy into electrical power, but rather sets the blade pitch angle and rotor speed corresponding to the mean

229 operational point.

230 The aerodynamic thrust on the rotor under different inflow wind speeds should be checked. The rotor was placed

231 in the plane of the calibrated wind field (x=5.2 m), and the hub center was located at y=0 m, z=0 m. Through a

232 six-component force sensor, the nacelle was connected to a rigid tower that was fixed on land. Unlike the flexible

233 stiffness-matched tower model used in the test process, a rigid tower with great wall thickness was used in the rotor

234 thrust calibration to ensure that no deformation occurred. This was to make the tower-top shear force measured by the

235 six-component force sensor equal to the aerodynamic thrust, not including the gravity component of the tower-top

236 structure and inertial force, which were caused by the deformation of the flexible tower. Constant winds with different

speeds were generated in turn by the wind generation system and applied to the rotor. The aerodynamic thrusts caused by inflow winds were recorded and compared with the target thrusts for the prototype-scale DTU reference rotor [8] in Fig. 13. The mean values of the measured and targeted rotor thrust under different wind speeds show good agreement. The time series of the measured rotor thrust under three different wind speeds (9.0 m/s, 11.4 m/s and 14.0 m/s) are shown in Fig. 14 (a), and it can be seen that the rotor thrusts show obvious vibrations. The PSD in Fig. 14 (b) shows thrust variations mainly at 1P and 3P, with small components in the low-frequency range and a component at approximately 0.4 rad/s under all three wind speeds. All of these responses are discussed in detail in Section 5.
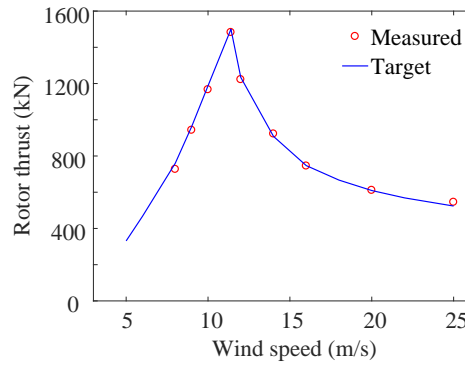

Figure 13: The measured and targeted mean values of rotor thrusts for bottom-fixed rotor under different wind speeds in full-scale.
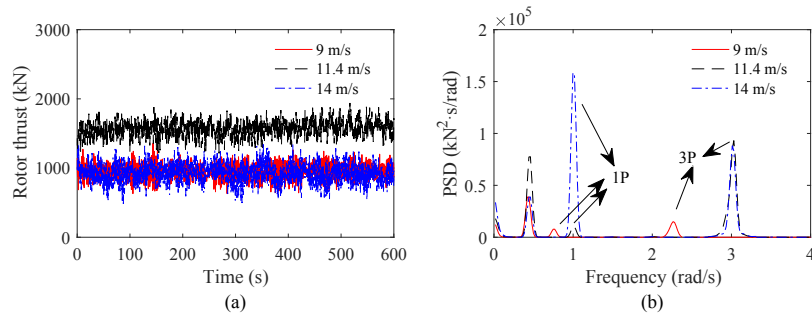

Figure 14: Full-scale (a) time series and (b) power spectra of the measured rotor thrust for bottom-fixed rotor under EC1, EC2 and EC3.

3.3. Tower model

This study adopted a stiffness-matched tower [30] to ensure that the natural frequency and deformation of the tower model structure are similar to the prototype one (following Froude scaling). A hammer test was conducted to check the vibration properties of the stiffness-matched tower model, including the natural frequency and damping. In the hammer test, an accelerometer arranged at the middle of the flexible tower was used to measure the vibration acceleration of the model. The tower was connected to the platform through a six-component force sensor. The rotor model, nacelle

16

250 model and other sensors were all installed on the tower-top, to ensure that the mass of the tower-top was accurate. An

251 impulse excitation was applied to the tower in the fore-aft direction by a hammer. The hammer test was conducted in

252 water where the platform was floating and connected to the mooring system. The time series of the vibration-induced

253 accelerations were recorded in Fig. 15. The decay frequency of 2.4 rad/s represents the damped natural frequency of

254 tower vibration.

255   The damping of the tower fore-aft vibration was tuned according to the results of the hammer test. The vibration

256 acceleration was compared with the results from the experimental hammer test in water, and the tower 1st fore-aft

257 mode structural damping ratio was adjusted until a match between the numerical and experimental decay time series

258 was obtained. The vibration acceleration comparison between the experimental and numerical decay results is shown

259 in Fig. 15. The calibrated damping ratio (1%) was used in the following simulations under a series of more complex

260 environmental conditions, to see the high-frequency tower vibration responses.
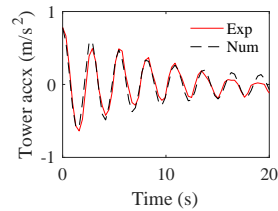
Figure 15: Vibration acceleration comparison between experimental and numerical results in the hammer test in water.

261 *3.4. Platform model and mooring model*

262   To correctly obtain the hydrodynamic force applied to the model, the platform model was scaled through Froude

263 scaling rules, which means that it was geometrically-matched. By adjusting the weights and positions of the iron or

264 lead ballast in the side columns and pontoons, the weight, center of gravity, and inertia of the FWT platform can be

265 accurately modeled.

266   For the mooring system, Fig. 16 illustrates the mooring line model used in the experiment, and the main parameters

267 are given in Table 2. The iron chains and lead wires were used in the experiment to adjust the weight of the mooring

268 line. A homogeneous iron chain was selected with the length of geometrical similarity, and lead wires were placed

269 in certain places with the same interval, so that the wet weight of the model-scale and prototype-scale mooring lines

270 matched. On this basis, a series of lead wires were arranged at each required position to correctly simulate the wet

271 weights of the clump weights. The experiment did not scale the outer diameter of each line directly. The stiffness of

272 the mooring line was adjusted by a spring, and a tensile test was conducted to ensure that the EA of the model-scale

273 mooring line was correct.

274   To calibrate the horizontal restoring stiffness of the mooring system, the relationship between the horizontal forces

275 and offsets was obtained in both experimental and numerical simulations, as shown in Fig. 17. The numerical results

17

Figure 16: A produced mooring line model used in the experiment.

are in good agreement with the experimental results. The force-offset relationship is fairly linear for offsets less than 10 m and slightly nonlinear for the offsets larger than 10 m.
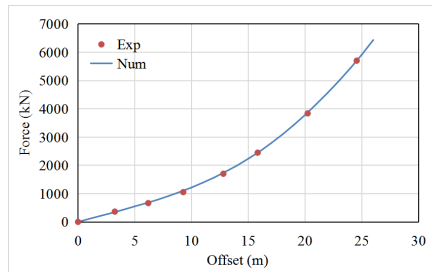

Figure 17: Horizontal restoring stiffness curve in the X-direction.

Free decay tests were conducted to calibrate the natural periods and viscous damping of the motions of the entire FWT system. The measured and numerical time series of decay tests for heave motion, surge motion, pitch motion and, yaw motion of the SPIC wind turbine concept are illustrated in Fig. 18 after tuning quadratic damping coefficients. The natural periods and damping of these motions were all simulated accurately by numerical software.

4. Numerical model and simulations

4.1. Fully-coupled wind turbine model and simulation

In this research, time-domain dynamic response analysis of the FWT was realized using the FAST v8 code [33]. The equation of motion in the time-domain is written as:

$$[\mathbf{M} + \mathbf{A}(\infty)]\,\ddot{\mathbf{x}}(t) + \int_0^t \mathbf{K}(\tau)\dot{\mathbf{x}}(t-\tau)d\tau + \mathbf{C}\mathbf{x}(t) = \mathbf{F}^{Wave} + \mathbf{F}^{Aero} + \mathbf{F}^{Drag} + \mathbf{F}^{Mooring}, \tag{2}$$

In the above equation, $\mathbf{M}$ represents the mass matrix; $\mathbf{A}(\infty)$ refers to the high-frequency limit of the added mass matrix; $\mathbf{C}$ represents the linear-restoring matrix. Eq.(2) uses convolution integral to express the retardation effect of free surface. $\mathbf{K}(\tau)$ refers to the retardation function. $\mathbf{x}$, $\dot{\mathbf{x}}$, and $\ddot{\mathbf{x}}$ are the vectors of motion, velocity, and acceleration,
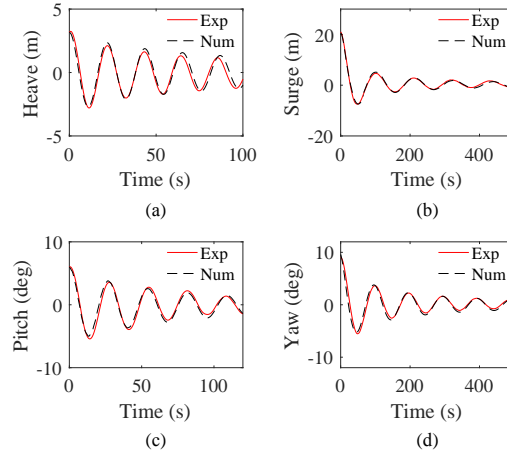
18

Figure 18: The time series of decay tests for (a) heave motion, (b) surge motion, (c) pitch motion, and (d) yaw motion.

respectively. $\mathbf{F}$ is the force applied to the floating wind turbine, including the hydrodynamic forces $\mathbf{F}^{Wave}$, aerodynamic loads $\mathbf{F}^{Aero}$, drag forces $\mathbf{F}^{Drag}$, and mooring forces $\mathbf{F}^{Wave}$. The simulations were carried out in full scale. The hydrodynamic coefficients on the left side of the Eq.(2) were all provided by the frequency domain calculation in HydroD [34]. In this study, there are no incident waves, so the wave force $\mathbf{F}^{Wave}$ can be neglected. In general, this coupled aero-hydro-servo-elastic-mooring problem was solved through the Runge–Kutta method.

4.1.1. Aerodynamic loads

AeroDyn [35], from NREL, was adopted to calculate the aerodynamic loads acting on the rotor based on the blade element-momentum (BEM) theory [36]. Both the actuating disc model and the independent blade element model in the blade element-momentum method are based on some idealized assumptions, which are somewhat different from the actual conditions of the offshore FWTs. Prandtl's tip loss factor and hub loss correction model were used to modify the traditional momentum theory to take the influence of the wake vortex near the blade tip and blade root into account. In blade element-momentum theory, when the axial induction factor exceeds a certain value, the predicted result calculated by Glauert correction is closer to the actual measured value. In addition, the dynamic inflow model considered the time delay before load equilibrium was reached. The Beddoes-Leishman (BL) dynamic stall model was used to correct the aerodynamic characteristics of the airfoil when the relative inflow was unsteady due to platform motion and wind turbulence. In addition, AeroDyn module also calculates the aerodynamic loads applied to the tower structure.

4.1.2. Hydrodynamic loads

Using the potential flow theory based panel model established in HydroD [34], the radiation and diffraction potential can be obtained by calculating the integral equation satisfying a series of boundary conditions. Then, the frequency-dependent hydrodynamic coefficients, including the added mass, potential damping, first-order and second-order wave force transfer functions can be obtained. The restoring force is influenced by the floating body motion and the restoring

19

matrix, which is determined by the properties of the wind turbine structure distribution. In addition, the viscous drag force acting on the floating platform which cannot be captured by the potential flow theory is calculated by the Morison's equation. In the case of wind only analysis in this paper, the first-order and the second-order wave excitation loads are not considered, while the radiation and the drag loads are considered.

4.1.3. Mooring system loads

The MoorDyn module [37] was used to calculate the loads applied by the catenary mooring system. It is based on the lumped-mass discretization of a mooring line. Each mooring line is made up of a series of evenly distributed segments, each segment is divided into two parts, and the properties of each part are lumped to the two adjacent nodes. The segments are replaced by damper spring systems. The model considers the axial stiffness, damping force, weight, buoyancy and hydrodynamic forces from Morison's equation (assuming still water so far), and vertical spring-damper forces from the contact with the seabed. MoorDyn adds point-mass and rigid-body objects to enable simulation of these hybrid-form mooring arrangements.

4.1.4. Operation mode

Table 5: Properties of two operation modes.

Item	Operation mode A	Operation mode B
Rotor speed	Fixed	Variable
Blade pitch angle	Fixed	Variable
Natural frequency of pitch controller	-	0.13 rad/s
Application	Considered both in model test and numerical simulation, with the purpose to compare the numerical and experimental results, and to to study the difference in responses from mode B.	Not considered in model test due to the limitation in experiment, but considered in numerical analyses to simulate the responses for realistic wind turbine and to study the difference in responses from mode A.

In this paper, two operation modes were introduced, as listed in Table 5. The operation mode conducted in the basin model tests was named "Mode A". Mode A maintained the rotor speed and blade pitch angle at fixed values corresponding to the mean wind speed. In Section 5, operation mode A was utilized in the numerical tests to simulate different conditions for comparisons with the experimental tests, to compare the dynamic performances of the wind turbine more clearly. However, in the real power production mode of the DTU 10 MW wind turbine, the control system following "Mode B" is composed of a variable speed generator torque controller and a collective blade pitch controller,

329 which provide real-time feedback. The wind energy can be converted into electrical power. For "Mode B", both the
330 rotor speed and the blade pitch angles varied with the relative wind speed. When the relative wind speed was below the
331 rated wind speed, the generator-torque controller actively adjusted the torque to tune the rotor speed, and the blade pitch
332 angles were fixed at zero to maximize the capture of power. At over-rated wind speeds, the rotor speed was adjusted
333 around 9.6 rpm through tuning the torque by the generator-torque controller, and the pitch angles were regulated by
334 the blade pitch controller to trace constant power output at 10 MW. When the speed exceeded the cut-out wind speed,
335 the rotor was controlled to be parked, and the pitch angle was set at 90 deg to minimize rotor thrust. The full-span
336 rotor-collective blade-pitch-angle commands are computed using gain-scheduled proportional-integrals (PIs). The pitch
337 controller used in Mode B reduced the natural frequency of the pitch controller from 0.38 rad/s (land-based) to 0.13
338 rad/s by modifying the proportional gains KP and integral gains KI, such that blade pitch controller natural frequency
339 is lower than the platform pitch frequency (0.24 rad/s). This avoids negative feedback effects in the platform pitch.

340 *4.2. Wind field model and simulation*

341 *4.2.1. Theory background*

342 A common wind field used in most numerical and experimental simulations is a constant uniform wind field, in
343 which the wind is constant in both time-scale and space-scale. However, the wind field in reality mostly has time-scale
344 wind speed variation and space-scale inhomogeneity.

345 Wind shear means that the wind speed varies vertically with the height. The power-law model is used to describe
346 the wind profile.

$$u(z) = u(\frac{z}{119})^{\alpha}, \tag{3}$$

347 where $u(z)$ is a function of z, it is the mean wind speed at any height; u is the mean wind speed at hub height; z is the
348 height above water level; α is an exponent parameter. The wind shear effect of the wind field is weaker as α decreases.
349 When α decreases to zero, the wind profile becomes uniform.

350 For a turbulent wind field whose wind speed varies with time, the time series of the longitudinal wind speed are
351 commonly generated according to the wind spectrum in the longitudinal direction. This study utilizes the IEC Kaimal
352 turbulence model [38]:

$$S_1(f) = \frac{4\sigma_1^2 L_1/u}{(1 + 6fL_1/u)^{5/3}}, \tag{4}$$

353 where f is the frequency, u is the mean wind speed at hub height, σ_1 is the standard deviation of the wind speed and L_1
354 is defined by the turbulence scale parameter. The turbulence intensity (TI) is expressed as $\sigma/u \cdot 100\%$. The turbulence
355 level of the wind field is weaker as TI decreases.

356 The wind field is described as nonuniform if there are spatial variations at a given time instant related to the
357 fluctuating part of the wind velocity. This spatial characteristic can be represented by the coherence, which describes
358 the correlation between two wind time series in the main wind direction at a certain separation distance in the lateral or

21

vertical direction at different frequencies:

$$Coh_{i,j}(f) = \frac{S_{i,j}(f)}{\sqrt{S_i(f)S_j(f)}}, \tag{5}$$

where $S_i(f)$ and $S_j(f)$ are one-side auto-spectra of wind velocities at two points i and j, and $S_{i,j}(f)$ is the cross spectrum between these two points. The coherence could be split into a real part called the co-coherence, and an imaginary part called the quad-coherence. The inhomogeneity of the wind field is more significant as the spatial coherence is closer to zero. When the spatial coherence increases to 1, the wind speed at each point in the wind field plane is totally identical at each time instant, and the wind field becomes a uniform one. Existing design standards for FWTs refer to the IEC-61400-1 standard [39], which suggests two possible models for generating space-scale turbulent numerical wind fields: 1) the Kaimal spectral and exponential coherence model (here called "Kaimal") [40], and 2) the Mann uniform shear model (here called "Mann") [41]. Both turbulent models, Kaimal and Mann, use the Kaimal spectrum in Eq. (4). The main difference between the approaches is related to the spatial coherence.

1) The Kaimal spectrum and exponential coherence model

The Kaimal spectrum and exponential coherence model recommended by the IEC utilizes a two-parameter exponential coherence model for the wind velocity in the mean wind direction. However, no coherence is modeled for the lateral and vertical velocity components. The coherence for the velocity in the mean wind direction is given as:

$$Coh_{i,j}(f) = \exp\left(-12\sqrt{\left(\frac{fr}{v}\right)^2 + \left(0.12\frac{r}{L_c}\right)^2}\right), \tag{6}$$

where f is the frequency, v is the mean wind speed at hub height, and r represents the distance between two points i and j. L_c is the coherence scale parameter.

2) The Mann uniform shear model

The Mann uniform shear model is based on a combination of rapid distortion theory (RDT) with assumptions that the isotropic energy spectrum is rapidly distorted by a uniform mean velocity shear. It uses a velocity spectral tensor to describe the coherence in three dimensions [41]. The Mann model is based on three parameters: $\alpha\varepsilon^{2/3}$, l, and γ. The parameter $\alpha\varepsilon^{2/3}$ is the Kolmogorov constant multiplied by the rate of the viscous dissipation of specific turbulent kinetic energy to two thirds, l is the isotropic turbulence integral scale parameter, and γ is the nondimensional parameter related to the lifetime of the eddies. The IEC standard [39] gives some guidelines regarding the input for the Mann model to obtain the Kaimal spectrum.

4.2.2. Wind field simulation

Some standard wind fields with different wind speeds and uniformity were simulated through the Turbsim [42] and Mann 64-bit turbulence generator [43]. The standard parameters can be adjusted including shear profile, mean wind speed, TI and spatial coherence. In the following simulation cases, the simulated time length was three hours. The first 720 seconds of the recorded data were removed to eliminate the transient part of the response. In TurbSim, all the wind field models were generated using the same grid height and grid width of 200 m. The wind fields were generated

22

at 32 grid points in the lateral and vertical directions with a spacing of 6.25 m. The time step in TurbSim was set as 0.08 seconds. The hub height of 119 m was defined to set the grid center at this position. The Mann 64-bit turbulence generator was used to generate a wind field as a three-dimensional box with $131072 \times 32 \times 32$ nodes and a grid size of 6.25 m in the vertical and lateral directions. Similar to TurbSim, the created Mann model wind field had enough grid points to cover the entire rotor area of the wind turbine. In the longitudinal wind direction, the grid size d_x was determined by the mean wind speed and found as follows:

$$d_x = \frac{T \cdot \bar{u}_x}{N_x},\tag{7}$$

where $\bar{u}_x$ is the mean wind speed, T is the total time, and N_x is the number of grid points in the longitudinal direction, which should be 2^n. To obtain a similar time step as TurbSim (0.08 s), an integer of 17 was chosen. The time step was given by dividing the simulation length of T by N_x, which resulted in a time step of 0.08 s.

5. Comparisons of experimental and numerical results under different wind conditions

The dynamic responses of the SPIC wind turbine concept in model tests and numerical simulations, including aerodynamic force, the tower-top shear force in the x-direction (TFx), tower-base bending moment around the y-axis (BMy), pitch motion and surge motion, nacelle acceleration in the x-direction (Naccx) are compared under the six wind-only conditions described in Table 4. The settings of the rotor speed (RS) and blade pitch angle (BP) under different conditions in model test and numerical simulation are listed in Table 6. The settings for experimental model are expressed in model-scale and the settings for numerical model are expressed in full-scale. And the temporal and spatial characteristics of the wind fields used in the numerical simulations are also given in this table, which would be interpreted in detail in the following sections. Each basin model test case lasted for approximately 25 minutes, corresponding to 3 hours for the prototype, and the sampling frequency was set to 25 Hz. The numerical test ran a 3-hour simulation with a sampling frequency of 3.125 Hz for each case. Numerical simulations were performed for the full-scale structure, which were then compared with the upscaled measurements from the model test. The measurements in the model test were upscaled to full-scale following Froude scaling, with the scaling ratio λ of 64. The scaling factors between model and prototype wind turbine system is different for various measurements, as seen in Table 7. In addition, since the actual floating wind turbine works in sea water and the model test is carried out in fresh water, so the density difference between sea water and fresh water should be taken into account. Generally, the density correction factor γ is 1.025. The data in the first 720 seconds were removed for both experimental and numerical results, to eliminate transients.

5.1. Comparisons of aerodynamic thrust force

The aerodynamic force obtained under each environmental condition was firstly compared with the model test results. The tower-top shear force was measured in the model tests. The measured data contain not only aerodynamic

23

Table 6: Experimental and numerical settings of the rotor speed (RS, unit: rpm) and blade pitch angle (BP, unit: deg); and temporal and spatial characteristics of the wind field generated in numerical simulations.

| Target wind type | EC | Exp | | Num | | Temporal variation of wind speed in numerical simulation | Spatial variation of wind speed of the main direction in numerical simulation |
		RS	BP	RS	BP		
Constant &uniform	EC1	76.8	0	9.6	0	Measured wind speed time series at 81 points (in calibration test)	Wind speed at 81 points +interpolation
Constant &uniform	EC2	57.8	0	7.2	0	Measured wind speed time series at hub point (in calibration test)	Uniform
	EC3	76.8	6	9.6	8.5		
	EC4	0	90	0	90		
Time-varying &uniform	EC5	76.8	0	9.6	0	Measured wind speed time series at hub point (in calibration test)	Uniform / Partially coherent (Similar coherence as EC1) / Incoherent
	EC6	76.8	0	9.6	0		

Table 7: Scaling factors of model scale measurements. (λ=64, γ=1.025)

Measurement	Formula	Scaling factor
Pitch motion	ϕ_s/ϕ_m	1
Surge motion	L_s/L_m	λ
Tower top shear force	F_s/F_m	$\gamma\lambda^3$
Tower base bending moment	M_s/M_m	$\gamma\lambda^4$
Nacelle acceleration	a_s/a_m	1
Time	T_s/T_m	$\lambda^{1/2}$
Frequency	f_s/f_m	$\lambda^{-1/2}$

thrust but also gravity components and inertial forces. Therefore, they should be separated from the measured force and then the aerodynamic force should be compared with the numerical results directly. In the model test, pitch motions were measured, so the gravity component of the tower-top can be estimated. The nacelle accelerations were also measured, so the inertial force of the tower-top can be calculated as well. Then the aerodynamic forces were approximately derived. The same measurements can also be realized through FAST. Then the aerodynamic thrust force under these wind-only conditions can be compared between the numerical and experimental conditions. The mean values, standard deviations and maximum values of the experimental and numerical aerodynamic force under EC1-EC6 are shown in Table 8.

Table 8: The mean values, standard deviations (STDs) and maximum values of the experimental and numerical aerodynamic force under EC1-EC6.

Statistics	Item	EC1	EC2	EC3	EC4	EC5	EC6
Mean	Exp	1.529E+03	9.660E+02	9.218E+02	1.460E+02	1.595E+03	1.571E+03
(kN)	Num	1.499E+03	9.636E+02	9.181E+02	1.543E+02	1.541E+03	1.521E+03
STD	Exp	1.123E+02	4.659E+01	1.572E+02	6.913E+01	2.084E+02	4.050E+02
(kN)	Num	8.955E+01	3.012E+01	6.288E+01	5.366E+01	1.976E+02	3.856E+02
Maximum	Exp	1.739E+03	1.097E+03	1.203E+03	3.802E+02	2.559E+03	3.034E+03
(kN)	Num	1.800E+03	1.070E+03	1.190E+03	3.980E+02	2.560E+03	2.970E+03

5.1.1. Constant wind condition

5.1.1.1. Rated wind condition

Due to the importance of the rated wind condition, the wind speed time series at 81 points in the wind field of EC1 were recorded in the wind field calibration test introduced in Section 3.1. Fig. 9 and Fig. 10 indicate that the experimentally generated "constant" wind also had a small turbulence intensity at low-frequency range, and the wind field is not perfectly uniform but the co-coherence is close to one. When establishing the numerical model of the wind field, the measured wind speed time history of 81 points can be defined in Turbsim to realize more accurate wind field simulation, as expressed in Table 6. Then, numerical simulations were conducted under this wind field. The aerodynamic thrust force under rated wind-only conditions can be compared between the numerical and experimental conditions, as seen in Fig. 19. The mean thrust forces of the model tests and numerical simulations show agreement. However, the times series of the aerodynamic force do not totally match. One reason is that the wind speed time series input in the numerical simulation was measured in the calibration test, rather than in the basin test. Therefore, the power spectra comparison is relatively important. Because the wind in EC1 shows small low-frequency component,

the aerodynamic thrust force is also excited at surge and pitch natural frequencies. The dynamic responses of the experimental and numerical results shown in PSD are basically identical except for the component at 0.4 rad/s. The experimental realizations with wind show responses at 0.4 rad/s. Compared with some other wave-only cases or current-only cases, only cases with wind show this response. Additionally, the shutdown cases that will be mentioned later do not show this spectral peak. Therefore, the appearance of this peak at 0.4 rad/s is thought to be associated with the operation of the motor in the nacelle. During the model tests, a torque sensor was mounted between the motor and the rotor, and the PSD of the measured motor torques under EC1 is shown in Fig. 20. Considerable responses can be seen at 0.4 rad/s under rated wind conditions. The component excited by the motor as an external excitation is not captured by the numerical model, and can be considered to be special experimental factor.
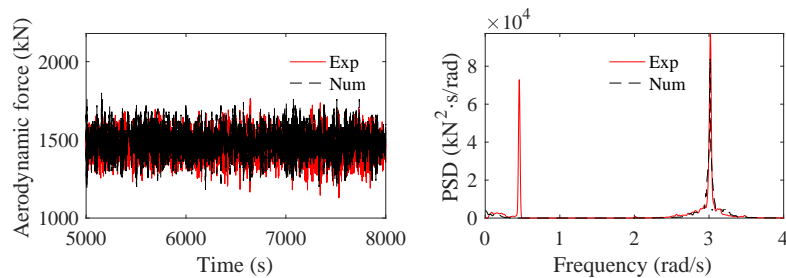
Figure 19: Comparisons of time series and power spectra of the aerodynamic thrust force between the experimental and numerical tests under rated wind condition EC1.
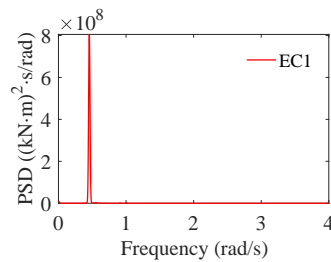
Figure 20: Experimental power spectrum of the motor torque in EC1.

5.1.1.2. Below-rated and over-rated wind condition

Two wind-only conditions with below-rated wind speed (9 m/s) and over-rated wind speed (14 m/s) were simulated in the model tests in sequence. Due to the limitation of the test time, the wind speeds at 81 points under EC2-EC5 were not all measured and only the wind speed at the hub point was recorded. Therefore, for these cases, the wind fields generated in the numerical model were assumed to be spatially uniform initially, and the wind speed at the hub point was input into InflowDyn. Then, the aerodynamic thrust forces were compared with the model test results in Fig. 21.

For below-rated wind speed conditions, the aerodynamic thrust force was decreased by reducing the rotor speed for
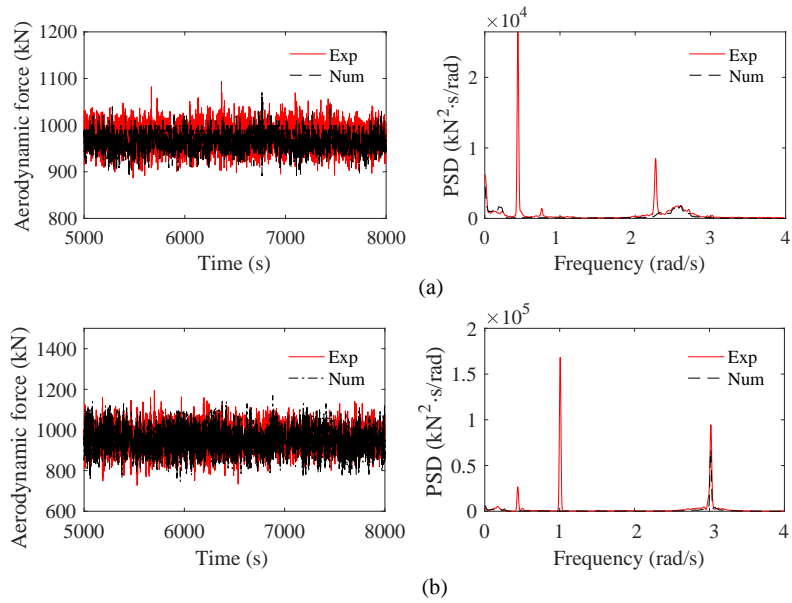
26

Figure 21: Comparisons of time series and power spectra of the aerodynamic thrust force between the experimental and numerical tests under (a) below-rated wind condition EC2 and (b) over-rated wind condition EC3.

the lower wind speed, and the mean value of aerodynamic thrust force was simulated accurately by a numerical model. The low-frequency responses caused by the slight turbulence of inflow wind are seen. In addition, the high-frequency responses caused by tower vibration are also obvious under constant below-rated wind condition. The differences in PSD also appear at frequency of 0.4 rad/s. Another significant difference between the experimental and numerical aerodynamic thrust forces appears at approximately 2.3 rad/s in Fig. 21 (a). The model test result shows a higher peak at a frequency of 3P. It is influenced by the nonuniformity of the experimental wind field as well. In a wind field with partial spatial coherence, each blade experiences fluctuations during the rotation process because of space-scale turbulence. Therefore, a 3P response is induced. For the uniform wind field, the wind speed at each point is identical at a certain time, but it varies in the time-scale. Therefore, in numerical simulation, if the wind field is modelled as a totally uniform one, a smaller 3P response can be captured. The 3P responses are larger when the wind field becomes less uniform.

In Fig. 21 (b), the mean aerodynamic thrust forces in numerical simulations and model tests were verified to be equal under over-rated wind conditions. However, the numerical simulation did not capture the 1P responses seen in the experimental spectra. The 1P responses are not obvious in the rated and below-rated wind speed conditions. For over-rated wind speed condition, to decrease aerodynamic thrust, blade pitch angles are no longer set as 0 deg. In the model test, if the blade pitch angle of each blade is not totally identical because of the imperfect installation, some influences may be present at the rotating frequency. Two numerical cases with and without this individual blade installation error are compared to verify this effect. In Case1 (without individual blade installation error), the blade

27

pitch angles are all set as 8.5 deg, whereas in the Case2 (with individual blade installation error), the pitch angles of the three blades are set as 7.5 deg, 8.5 deg and 9.5 deg. The rotor speeds for the two cases are both fixed at 9.6 rpm, corresponding to a rotating frequency (1P) of nearly 1 rad/s. The effects of individual blade installation are present through an examination of the time series and PSDs of aerodynamic thrust force in Fig. 22. The effect of individual blade installation on the mean value of aerodynamic thrust force is not significant. Under a uniform but spectral wind field with a little turbulence, aerodynamic thrust force is slightly excited at the 3P frequency, which is caused by rotor rotation. When individual installation error occurs (Case2), that is, the pitch angles of the three blades are not exactly the same, the aerodynamic thrust force will be obviously excited at the 1P frequency. This is because different pitch angles among the three blades can induce different normal forces and tangential forces when applied to each blade in the rotation process. The change at 1P is induced by periodic changes in the moment of rotor thrust. In the numerical simulation, the pitch angles of the three blades are guaranteed to be equal and accurate at every moment, so 1P responses cannot be captured. Therefore, this response difference at the 1P frequency is also caused by experimental factors, which are not present in the numerical model.
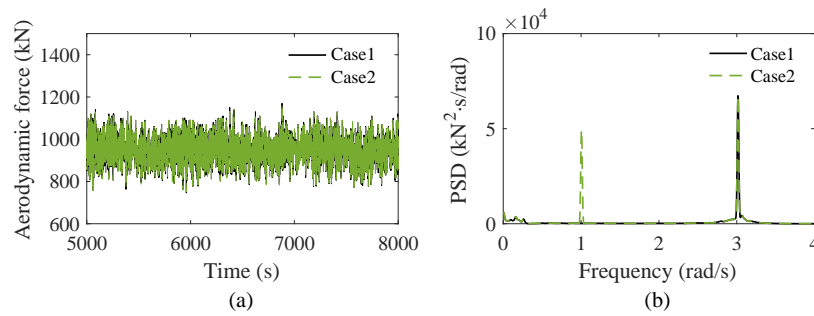
Figure 22: Effect of individual blade installation on (a) time series and (b) power spectra of the aerodynamic thrust force under over-rated wind condition (Case1: Without individual installation error; Case2: With individual installation error).

5.1.1.3. Parked condition

A wind-only condition with over-cut-out wind speeds was also simulated in the model test. The wind speed time series at hub point measured during the calibration test were input to the InflowDyn of FAST and the wind field was also set as a uniform wind field. For this over cut-out wind speed condition, the blade is feathered and the wind turbine is shut down, so the drag force of the wind acts more on the tower at this time. Therefore, a layer of foam ring was used to cover the tower outer surface. The outer diameter of the foam ring was directly scaled from the outer diameter of the full-scale tower. This may have a slight effect on the tower vibration natural frequency, but it will accurately simulate the drag force on the tower generated by the wind. The aerodynamic thrust force under EC4 was compared with the model test results in Fig. 23. By comparing the time series, the mean values of drag forces acting on the tower-top are simulated accurately. Under this extreme condition, the motor no longer provides any external excitation because the wind turbine is shut down. Therefore, the aerodynamic thrust force is not excited at a frequency of 0.4 rad/s. Because

28

the rotor speed is fixed at 0 deg, no 1P or 3P responses can be seen. Spectral peaks are significant at the pitch natural frequency and tower vibration frequency.
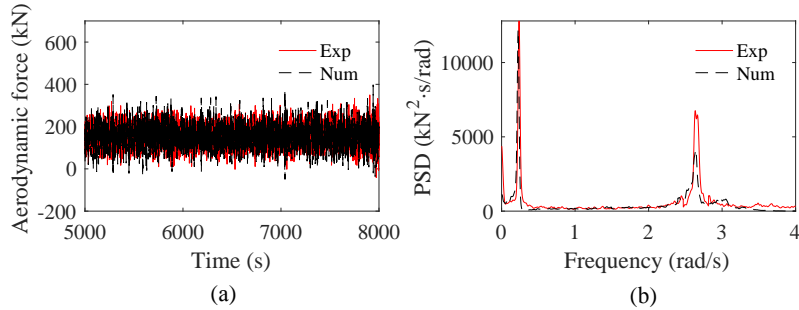

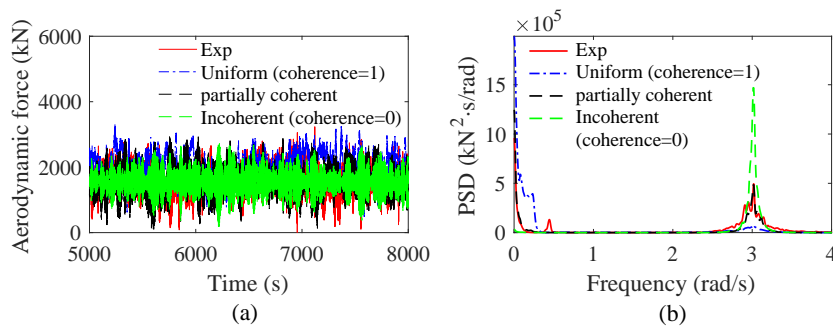Figure 23: Comparisons of (a) time series and (b) power spectra of the aerodynamic thrust force between the experimental and numerical tests under EC4.

5.1.2. Time-varying wind condition

Two time-varying wind-only conditions (EC5 and EC6) of rated speed were simulated in the model tests. The wind speed measured at the hub point in the calibration test was input to the InflowDyn of FAST, and the wind fields were set as uniform at the first stage. These measured time-varying winds, as shown in Fig. 11, presented obvious low-frequency components. Then, the aerodynamic thrust forces under EC6 were compared with the model test results in Fig. 24. The dynamic responses shown in PSD are different between the experimental and numerical results. Except for the different responses at 0.4 rad/s and 3P, obvious differences mainly appear in low-frequency responses. The low-frequency component of aerodynamic thrust force is induced by the low-frequency excitation of wind loads. The numerical results show larger low-frequency responses than the experimental results when the wind field was set as uniform. Based on this difference, some works were conducted to investigate what causes the difference in the comparison of aerodynamic thrust force. This might be related to two factors:

Figure 24: Comparisons of (a) time series and (b) power spectra of the aerodynamic force among experimental and numerical tests under three wind fields with different spatial coherence (Mean wind speed=11.4 m/s, and TI=14.6%).

a. Wind loads on the model-scale turbine model.

The C_t coefficients of the full-scale blade used in FAST and the performance-matched blade used in the model test are compared in Fig. 12. When this performance-matched blade was designed, C_t is mainly satisfactory under the rated condition. Therefore, under some other TSRs, C_t is still a little smaller. Under the time-varying wind, the relative wind speed varies all the time. In Fig. 12, the C_t of the full-scale rotor varies more than that of the performance-matched rotor, which means that in FAST, the aerodynamic thrust can be expected to show a higher spectral peak than in the model test. Therefore, this factor also influences the low-frequency aerodynamic thrust force.

b. Wind field generation.

The wind field is also an essential factor that affects the aerodynamic excitation force. It has been proved that the influence of the wind speed randomness can be eliminated. As mentioned above, the wind field in the numerical calculation was approximated as uniform field in the first step of this study. However, in conditions such as EC5 and EC6, the wind field generated by the wind generation system is not totally uniform because of some difference between each fan. Thus, in the next step, the effect of the wind field spatial coherence on the aerodynamic thrust force was also investigated. The rated wind condition EC6 with a TI of 14.6% was taken as an example. Three different wind fields were generated by TurbSim: (1) uniform wind field (spatial coherence=1); (2) turbulent wind field (partially coherent); and (3) completely incoherent wind field (spatial coherence=0). For wind field with partial coherence, the spatial coherence parameter "SCMod1" was set as GENERAL coherence model in Turbsim, and the coherence parameters were set to make the coherence similar to the value of EC1. For completely incoherent wind field, "SCMod1" was set as the NONE coherence model in Turbsim. Also, in these wind fields, the measured wind speed time series at hub point were defind as the input wind speeds. Then, these wind fields were input into InflowDyn to make simulations. Fig. 24 illustrates the effect of spatial coherence on the aerodynamic thrust force. As shown, the mean thrust forces of the numerical simulations is decreasing slightly when the coherence is closer to 0. The low-frequency responses increase substantially when the points in the wind field become completely coherent with each other. In two nonuniform fields, the wind speed at each point varies around the mean level of 11.4 m/s. Due to the phase difference, the speeds at some points are higher than 11.4 m/s, whereas others are lower. In this circumstance, the variation in the average wind speed seen by the rotor is relieved due to the phase lag at different points. The average wind speed across the rotor plane is close to 11.4 m/s, although it also varies with time. In contrast, the wind speeds at all points are in phase with each other for the uniform wind field. If the speed at the reference point (hub center) exceeds 11.4 m/s, then the speeds at all other points are higher than 11.4 m/s. Apparently, the inflow seen by the rotor is more unsteady in the presence of complete coherence. The low-frequency variations in the thrust force increase when coherence increases, as the rotor-averaged wind speed varies more. The 3P variations in the thrust decrease when coherence increases as the turbulence sampling effect disappears. In Fig. 24, when the wind field is regarded as a partially coherent one, the low-frequency and 3P components of numerical results and experimental results are the most similar. It can be concluded that the wind field in the model test is not uniform and that the spatial coherence indeed has a significant influence on the low-frequency aerodynamic thrust force.

30

5.2. Comparisons of other dynamic responses

The above content analyzes and explains the differences between the aerodynamic thrust obtained from the model tests and the aerodynamic thrust obtained from numerical simulations under six wind-only conditions. After the simulations of aerodynamic properties were verified, some other essential dynamic responses, including the tower-top shear force (TFx), tower-base bending moment (BMy), pitch motion, surge motion, and nacelle acceleration (Naccx), were also calibrated. Through the above analysis, it can be obtained that the average thrusts are simulated accurately by the numerical model, and the differences between the thrust spectra obtained by the numerical simulation and the experimental simulation are mainly caused by the difference in wind fields, the external excitation of the motor, and the individual blade installation error. Among them, the external excitation of the motor and the blade imperfect installation are test factors, which are not considered in the following numerical simulations. However, some adjustments have been made to the wind field models in the numerical simulations. The wind fields in time-varying wind conditions EC5 and EC6 were generated using the partially coherent model. On this basis, the mean values of the tower-top shear force, tower-base bending moment, pitch motion, surge motion, and nacelle acceleration (Naccx) under EC1-EC6 are obtained and listed in Table 9, and the power spectra are compared in Fig. 25 - Fig. 30.

Table 9: Comparisons of the mean values of tower-top shear force (TFx), tower-base bending moment (BMy), pitch motion, and surge motion between the experimental and numerical tests under EC1-EC6.

| Measurement	Item	EC1	EC2	EC3	EC4	EC5	EC6
TFx	Exp (kN)	2.349E3	1.342E3	1.400E3	1.813E2	2.295E3	2.254E3
	Num (kN)	2.324E3	1.348E3	1.424E3	1.766E2	2.307E3	2.276E3
	Relative error (%)	-1.064	0.447	1.714	-2.592	0.523	0.976
BMy	Exp (kN·m)	2.334E5	1.358E5	1.457E5	1.228E4	2.303E5	2.278E5
	Num (kN·m)	2.382E5	1.366E5	1.471E5	1.215E4	2.383E5	2.305E5
	Relative error (%)	2.057	0.589	0.961	-1.059	3.474	1.185
Pitch	Exp (deg)	5.085	3.028	3.133	0.252	5.015	4.852
	Num (deg)	5.049	3.058	3.176	0.247	5.053	4.894
	Relative error (%)	-0.708	0.991	1.372	-1.984	0.758	0.866
Surge	Exp (m)	6.953	5.011	5.629	3.970	6.937	6.814
	Num (m)	6.977	5.036	5.633	3.958	6.954	6.833
	Relative error (%)	0.345	0.499	0.071	-0.302	0.245	0.279
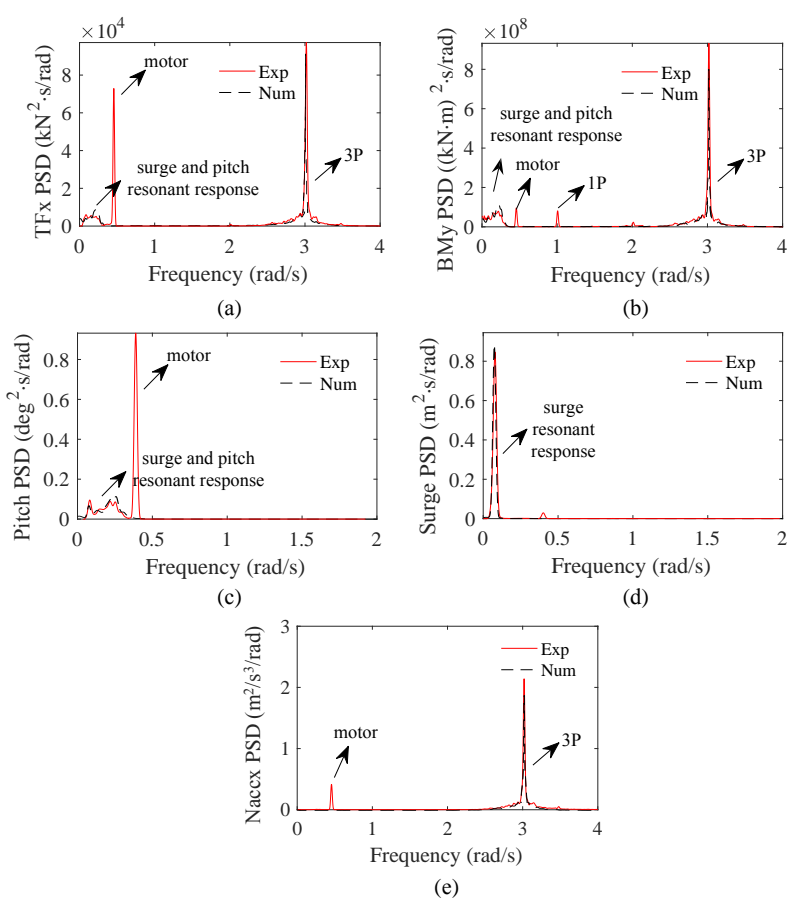
Figure 25: Comparisons of power spectra of (a) tower-top shear force (TFx), (b) tower-base bending moment (BMy), (c) pitch motion, (d) surge motion, and (e) nacelle acceleration

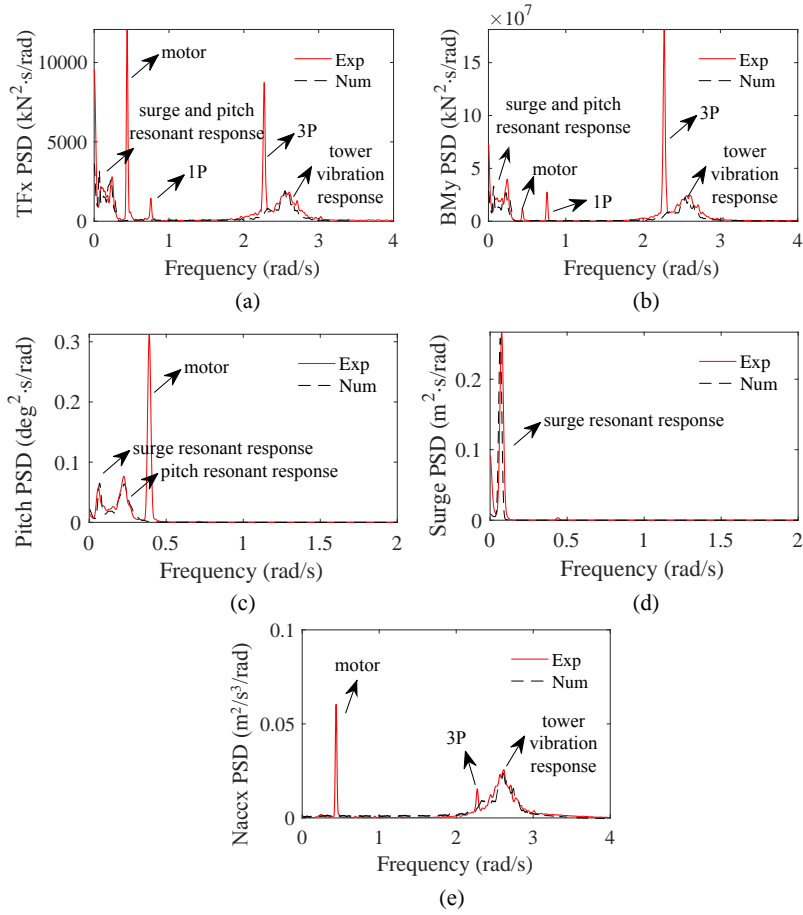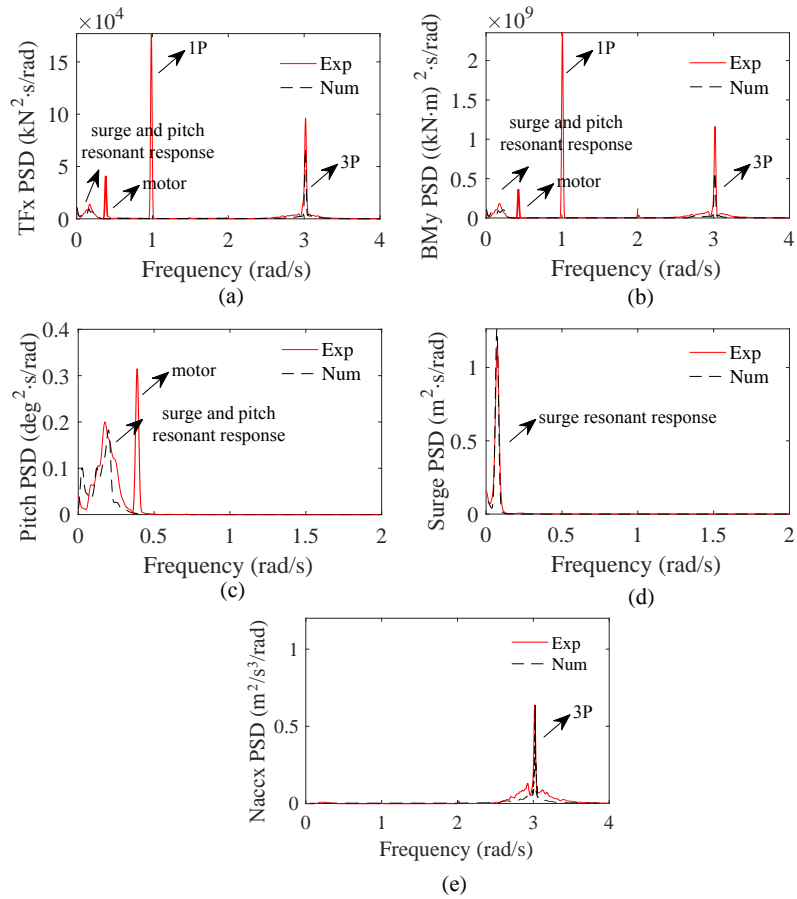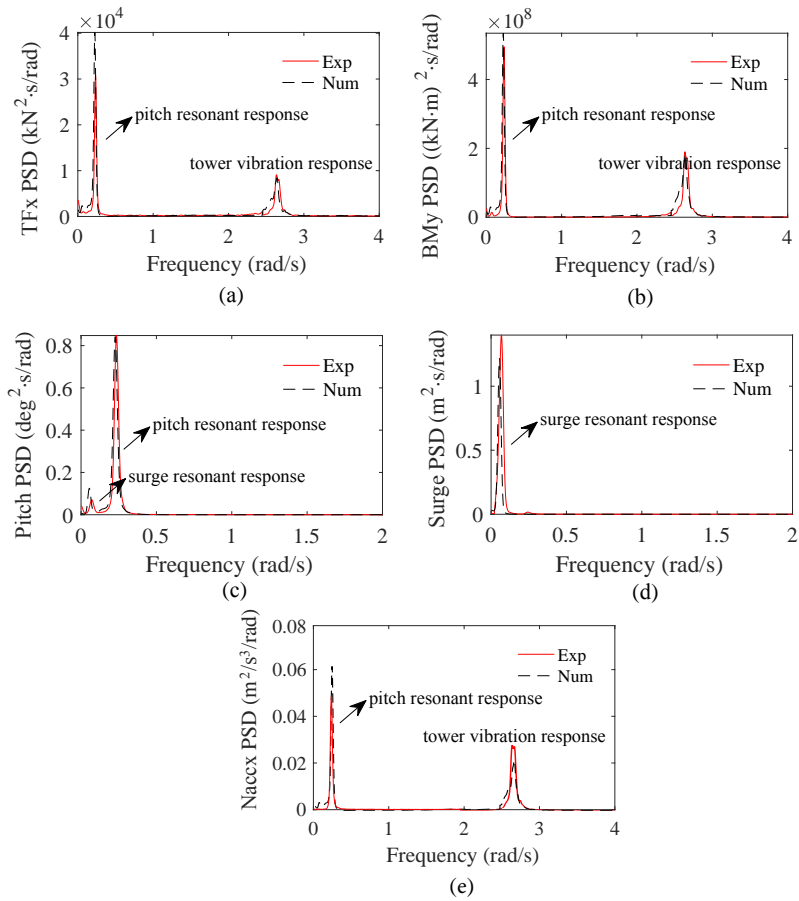between the experimental and numerical tests under EC1.

Figure 26: Comparisons of power spectra of (a) tower-top shear force (TFx), (b) tower-base bending moment (BMy), (c) pitch motion, (d) surge motion, and (e) nacelle acceleration

between the experimental and numerical tests under EC2.

6. Numerical analysis of the wind field effect on the SPIC wind turbine concept with the real operation mode

By carrying out an in-depth calculation and analysis of the dynamic responses of the SPIC concept 10 MW FWT under several different wind conditions, the comparison between the numerical simulation and the experimental results verified the validity of the numerical calculation model. However, there are some limitations from model tests, so it is necessary to conduct a series of numerical simulations to further see how large differences are when using different wind field models. This section conducts the numerical analysis for the dynamic responses and power generation performance of the SPIC concept FWT in four kinds of rated-speed wind fields, namely, "uniform and constant wind field", "shear and constant wind field", "uniform and spectral wind field", and "turbulent wind field". This can investigate the impact of wind shear, turbulence intensity and coherent structure of the wind fields, and enhance the performance verification of the SPIC wind turbine concept under more complex wind conditions.
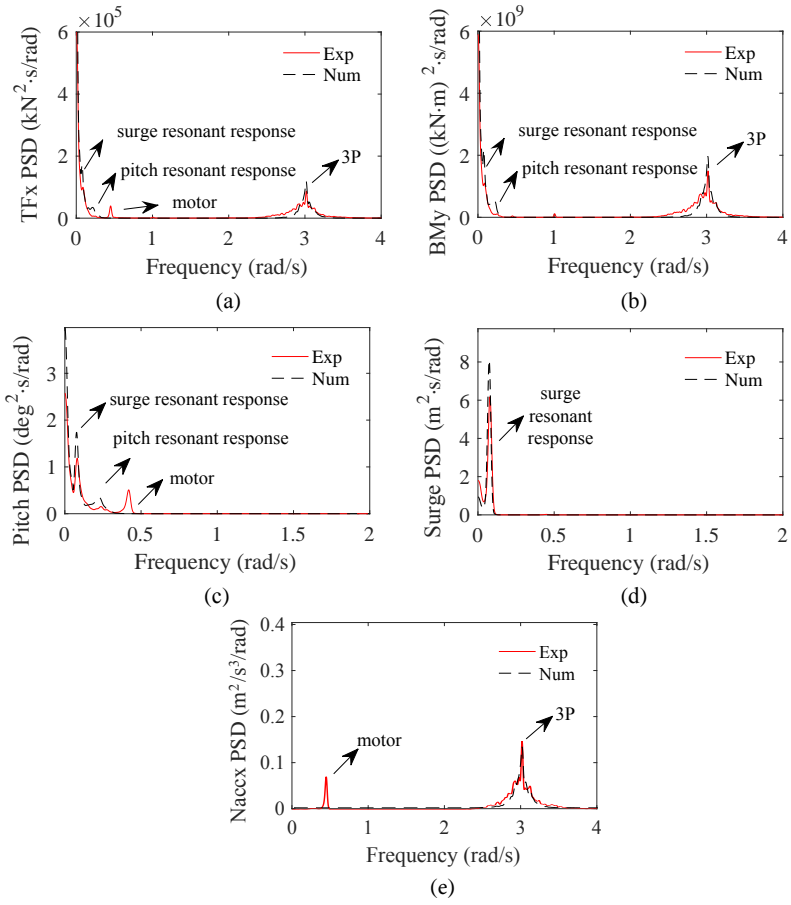
33

Figure 27: Comparisons of power spectra of (a) tower-top shear force (TFx), (b) tower-base bending moment (BMy), (c) pitch motion, (d) surge motion, and (e) nacelle acceleration

between the experimental and numerical tests under EC3.

Figure 28: Comparisons of power spectra of (a) tower-top shear force (TFx), (b) tower-base bending moment (BMy), (c) pitch motion, (d) surge motion, and (e) nacelle acceleration

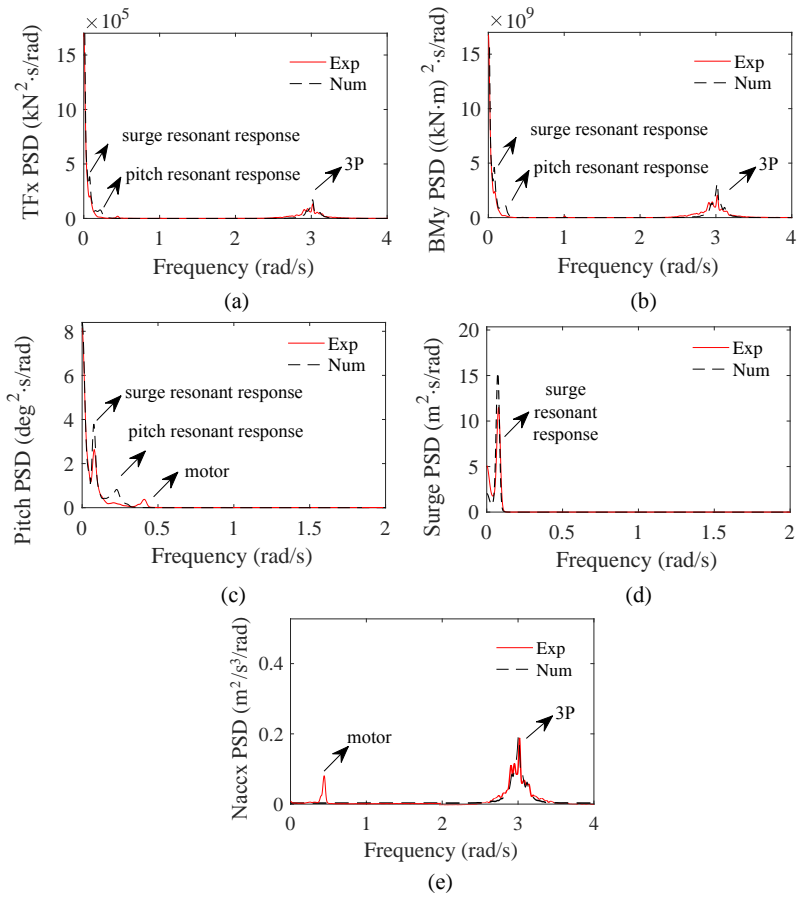between the experimental and numerical tests under EC4.

Figure 29: Comparisons of power spectra of (a) tower-top shear force (TFx), (b) tower-base bending moment (BMy), (c) pitch motion, (d) surge motion, and (e) nacelle acceleration

between the experimental and numerical tests under EC5.

Figure 30: Comparisons of power spectra of (a) tower-top shear force (TFx), (b) tower-base bending moment (BMy), (c) pitch motion, (d) surge motion, and (e) nacelle acceleration

between the experimental and numerical tests under EC6.

6.1. Influences of different operation modes

In this section, the operation mode in the numerical model needs to be adjusted first. It is well known that the wind turbine controller affects the dynamics of floating offshore wind turbines. To investigate the influences of two different operation modes mentioned in Section 4.1.4, discussions concerning the response differences under these two control mechanisms are to be achieved through numerical simulations before investigating the wind field effect. This study utilized the validated numerical model with Modes A and B to predict the dynamic responses of the SPIC wind turbine under turbulent rated wind condition EC6, respectively. The comparisons of the time series and power spectra of aerodynamic thrust force and pitch motion between two different control modes under EC6 are shown in Fig. 31.
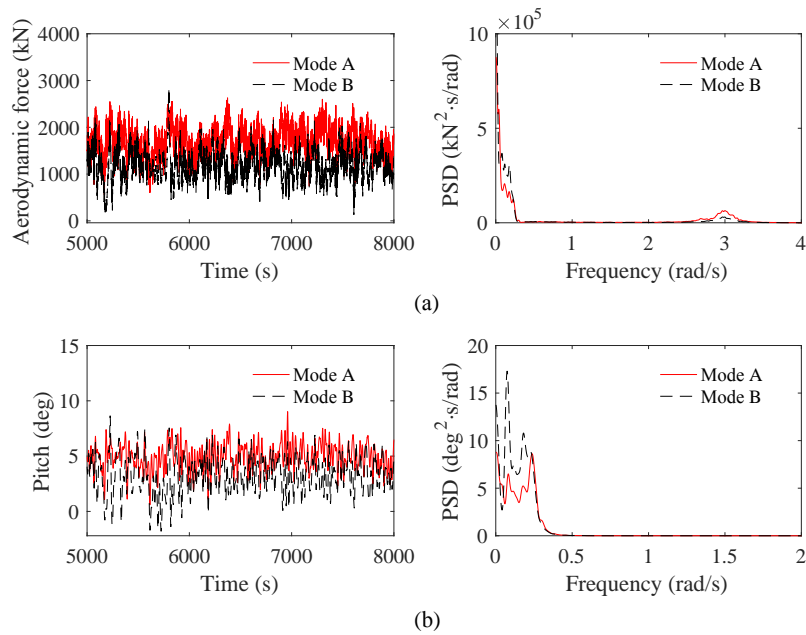

Figure 31: Comparisons of the time series and power spectra of (a) aerodynamic thrust force and (b) pitch motion between two different operation modes under a turbulent rated wind condition EC6.

Under EC6, the average values of aerodynamic thrust force and pitch motion for Mode B are smaller than those for Mode A. This is easy to understand because under Mode B, the aerodynamic thrust is decreased by the blade pitch controller when wind speed is over the rated value, and thrust is also decreased by the generator torque controller through the reduced rotor speed when wind speed is below the rated value. For spectral wind condition EC6, the effect of operation modes on the power spectra is significant. The influence can be seen in both the low-frequency range and high-frequency range. The aerodynamic thrust force and pitch motion show large peaks at the platform surge and pitch frequency, which are more pronounced for Mode B. In Mode B, the frequency of the pitch controller is smaller than the pitch natural frequency, which means that the pitch controller is detuned to avoid negative feedback. Mode A is an extreme detuning: The natural frequency of the blade pitch controller in Mode B is 0.13 rad/s, and this value is as low

38

as zero under Mode A. This means that the blade pitch mode in Mode A does not react to the changes in relative wind speed. According to the same logical analysis, Mode A can provide greater active damping than Mode B. Therefore, it can be seen that the low-frequency response under Mode A is smaller. In contrast, the variation in 3P is decreased by Mode B. Mode A has a fixed rotor speed, and thus a single 3P frequency, while Mode B gives variable 3P and more diffuse thrust variation.

6.2. Numerical analysis for wind field effect

In all subsequent numerical simulations, Mode B was chosen as the operation mode in the numerical model. Numerical analysis of wind field effects on the dynamic responses of the SPIC wind turbine concept is conducted under seven wind fields, as explained in Table 10. A uniform and constant wind field was seen as a reference wind field, which showed rated-speed at any moment and position. Two shear and constant wind fields with different power law exponent parameters, namely, "Shear1" and "Shear2", were used to study the wind shear effect. Two uniform and spectral wind fields with different turbulence intensities, namely "Turb1" and "Turb2", were chosen to see the turbulence intensity effect. Two turbulent wind fields with different spatial coherence models, namely, "Kaimal" and "Mann" were utilized to show the coherent structure effect. The detailed characteristics of these seven wind fields are introduced in the respective subsections.

Table 10: The properties of wind shear, turbulence intensity and coherent structure of seven simulated wind fields.

Wind field	Uniform and constant	Shear1	Shear2	Turb1	Turb2	Kaimal	Mann
Wind shear	$\alpha=0$	$\alpha=0.15$	$\alpha=0.25$	$\alpha=0$	$\alpha=0$	$\alpha=0$	$\alpha=0$
Turbulence intensity	TI=0%	TI=0%	TI=0%	TI=10.0%	TI=14.6%	TI=14.6%	TI=14.6%
Coherent structure	Uniform	-	-	Uniform	Uniform	Kaimal	Mann

6.2.1. Wind shear effect

Three wind fields with different wind profiles were selected to investigate the effect of wind shear. The first one is a uniform and constant one, with a wind speed of 11.4 m/s at every point and moment. The other two wind fields are constant but shear, with a wind speed at hub height of 11.4 m/s. The power law exponent α is set as 0.15 and 0.25, respectively.

Table 11 gives the mean values and standard deviations of the blade-root flapwise bending moment (BRM), tower-top shear force (TFx), generated power, and pitch motion under these three conditions. Although as the exponential parameter increases, the average value of each response decreases, the wind shear effect is limited. When a certain blade experiences a high-speed wind region above the hub height, other blades simultaneously experience a low-speed wind region below the hub height. Since the operation mode is collective blade pitch control, the resultant force

39

generated by the three blades is relatively stable. However, because the thrust is maximum when the wind speed is close to the rated speed, the thrust will be slightly larger when the exponential parameter is smaller. Therefore, the effect of shear force on the mean values of the blade-root bending moment, tower-top shear force, and pitch motion can be interpreted. An individual blade experiences wind speed variations during the rotation process in the shear wind field. Therefore, the tower-top shear force and blade-root bending moment experience increased fluctuation when the wind shear is more significant. Fig. 32 shows the power spectra of these responses. The effect of wind shear on the blade-root bending moment is seen at the 1P frequency, and the effect on the tower-top shear force is present at the 3P frequency. For generated power, the difference of mean values among three wind-only conditions is relatively larger. When the blade experiences a high-speed wind region above the hub height, the aerodynamic thrust is larger, while the generated power is maintained at 10 MW. When the blade is rotating to the low-speed wind region below the hub height, the generated power is smaller than 10 MW. Therefore, such a combined effect will make the total power have a smaller average value under a more sheared wind field. The generated power is also influenced by the wind shear effect at the 3P frequency, which is induced by the blade rotation.

Table 11: Comparisons of the mean values and standard deviations of blade-root bending moment (BRM), tower-top shear force (TFx), generated power, and pitch motion under seven different wind fields.

Measurement	Statistics	Uniform and constant	Shear1	Shear2	Turb1	Turb2	Kaimal	Mann
BRM	Mean	2.994E4	2.899E4	2.855E4	2.470E4	2.293E4	2.486E4	2.332E4
(kN·m)	Std.dev	1.070E3	1.081E3	2.066E3	4.401E3	5.772E3	4.191E3	4.732E3
TFx	Mean	2.081E3	2.034E3	2.016E3	1.695E3	1.569E3	1.707E3	1.595E3
(kN)	Std.dev	2.306E1	2.540E1	4.119E1	3.694E2	4.947E2	3.772E2	4.511E2
Power	Mean	9.999	9.856	9.740	9.365	8.930	9.408	9.723
(MW)	Std.dev	0.003	0.007	0.008	1.613	2.315	1.348	1.044
Pitch	Mean	4.544	4.541	4.538	3.673	3.392	3.699	3.443
(deg)	Std.dev	0.002	0.002	0.002	1.157	1.593	0.009	0.009

6.2.2. Turbulence intensity effect

The effect of turbulence intensity is examined by comparing the FWT performance among three rated wind conditions with different TIs (0%, 10%, and 14.6%). The red lines in Fig. 11 show the theoretical wind spectra of the two turbulent winds. For all three wind inflows, the power law exponent is set as 0 and the spatial coherence is set as 1, to eliminate the effects of wind shear and coherent structures.

Table 11 shows the mean values and standard deviations of the blade-root bending moment (BRM), tower-top shear
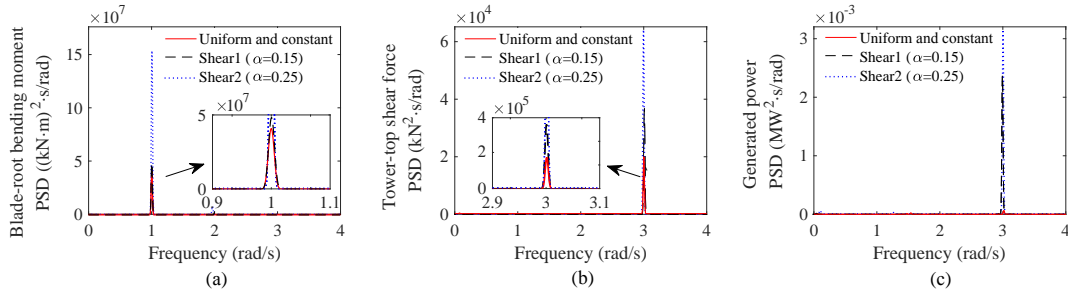
40

Figure 32: Comparisons of power spectra of (a) blade-root bending moment, (b) tower-top shear force, and (c) generated power under three wind-only conditions with different wind shears.

force (TFx), generated power, and pitch motion under three conditions. It is easy to identify that the mean values of all these responses decrease when the turbulence intensity increases. Although the mean wind speeds of the three wind inflows are identical, the wind with greater turbulence deviates more from the rated wind speed at each moment. When the wind speed is lower or higher than the rated wind speed, according to the real-time operation mode, the generated thrust is less than the rated thrust, as shown in Fig. 13. The larger the turbulence intensity is, the greater the range of thrust variation, and therefore the smaller the average value. Then, the decreasing trend of the average blade-root bending moment, tower-top shear force, and pitch motion can be interpreted. For the power generated, it decreases as the wind speed decreases when the wind speed is less than the rated value, and it is maintained at 10 MW when the wind speed is greater than the rated value. Therefore, its mean value is also smaller when wind speed varies more in time. Nevertheless, the standard deviation is augmented significantly by increasing inflow turbulence. To illustrate the turbulence intensity effect in more detail, Fig. 33 shows the power spectra of the blade-root bending moment, tower-top shear force, generated power, and pitch motion under three wind-only conditions with different turbulence intensities. Under constant and uniform wind condition, almost no power is excited at each frequency. Under turbulent wind conditions, all of the spectra are dominated by the low-frequency component, which is induced by the slow variation of wind speed in time-scale. The responses at the surge natural frequency and pitch natural frequency are significantly augmented when TI increases. In addition, 3P responses can be seen in the TFx spectra under two turbulent conditions due to the inflow velocity fluctuation during the rotation, and the responses are larger under more turbulent conditions. For power generation, the torque controller is operating to maximize the power generation in the below-rated condition and the blade pitch controller regulates the power generation at 10 MW in the over-rated condition. Therefore, the generated power is sensitive to the wind speed variation as well.

6.2.3. Coherent structure effect

The inhomogeneity of a wind field is also caused by spatial coherence, that is, the phase difference between two points in one wind field. The wind speeds are not uniformly distributed at each time instant for the partially coherent wind fields. This research selected two possible models for generating space-scale turbulent numerical wind fields: 1)
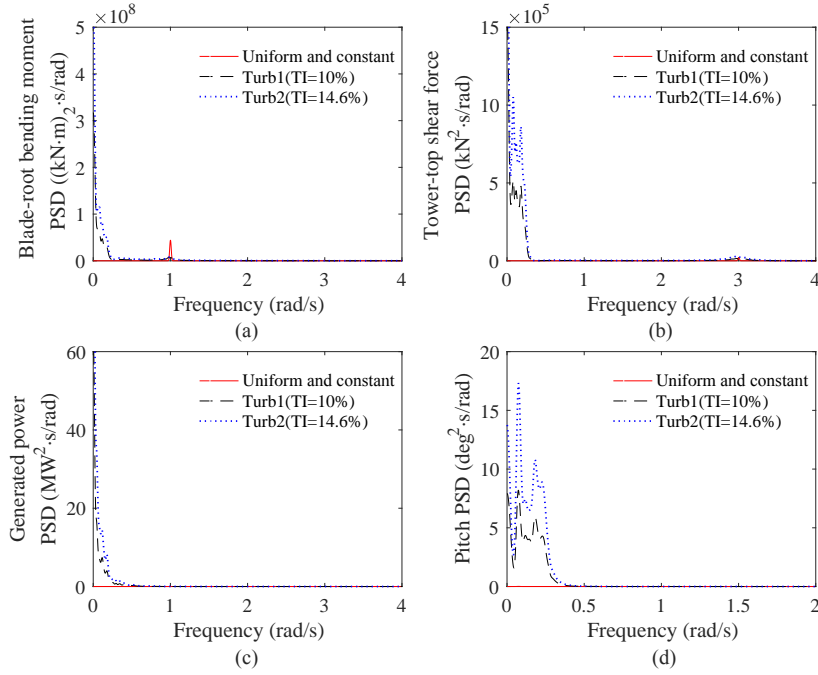
41

Figure 33: Comparisons of power spectra of (a) blade-root bending moment, (b) tower-top shear force, (c) generated power, and (d) pitch motion under three wind-only conditions with different turbulence intensities.

the Kaimal spectral and exponential coherence model (here called "Kaimal"), and 2) the Mann uniform shear model (here called "Mann"). As introduced in Section 4.2.1, both turbulent models, Kaimal and Mann, use the Kaimal spectrum in Eq. (4). The main difference between the approaches is related to the spatial coherence. The mean value of the wind speed time series of any point in these two wind fields is always 11.4 m/s, and the turbulent intensity is 14.6%. TurbSim and Mann 64-bit turbulence generator were used to generate the target "Kaimal" and "Mann" wind fields, respectively. The settings were described in detail in Section 4.2.2.

These two wind fields need to be studied before fully coupled numerical analysis. The two wind fields were compared in time-scale first. The hub center was selected as a reference point, and the wind speeds at the reference point of these two comparative wind fields are illustrated in Fig. 34. The wind speed time series differ greatly, but their mean values are identical. The power spectra are similar between the two different wind fields in the low-frequency range.

Then, the two wind fields should be compared at the spatial scale. The co-coherence mentioned in Section 4.2.1 was used to visualize the comparison between the generated Kaimal and Mann model wind fields as a function of frequency. The co-coherence of the wind speed component in the direction of the main wind direction (longitudinal component) at rated wind speed was assessed for both lateral and vertical directions at two different separation distances r defined by the rotor diameter D of the wind turbine: approximately 1/4 D and 1/2 D. The separation distances were chosen as 40 m and 80 m, respectively. Fig. 35 (a) illustrates the co-coherence comparisons between the Kaimal model and
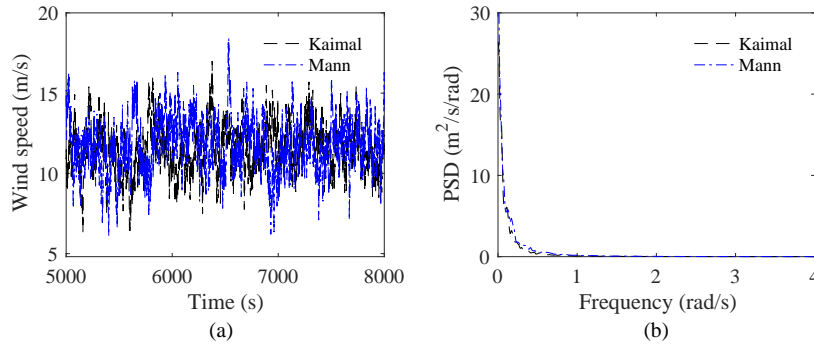
42

Figure 34: Comparisons of (a) time series and (b) power spectra between "Kaimal" wind and "Mann" wind.

Mann model. Some phenomena can be summarized. In terms of lateral co-coherence, the Mann model gives lower values than the Kaimal model regardless of the separation distance. The lateral co-coherence shows a decreasing trend when the separation distance increases, and the co-coherence of the Mann model falls more obviously than that of the Kaimal model. For vertical co-coherence, the values of two models are relatively closer to each other, and the co-coherence does not decrease drastically with the increasing separation distance for both two models. It can also be observed that the co-coherence of the Mann model is negative at some reduced frequency ranges, which is induced by an opposite phase of the longitudinal wind component for some frequencies. The dynamic loads acting on the wind turbine blade or rotor can be changed significantly by this effect. Fig. 35 (b) illustrates the quad-coherence comparisons between the Kaimal model and Mann model. The Kaimal model gives quad-coherence values close to zero regardless of the direction and separation distance. The wind velocity fluctuations are considered to be in the same phase. However, relatively larger quad-coherence values are observed for Mann model, especially in vertical direction. The corresponding phase shifts between two time series separated in space are expected to influence the responses of FWT.

To compare the coherent structure quantitatively, the proper orthogonal decomposition (POD) method [44] was also introduced to decompose these two wind fields. The POD method considers the longitudinal, lateral and vertical components (u,v,w) of wind velocity $\mathbf{u}$. The POD mode shape ϕ_k is associated with energy levels, and the lower modes contain higher energy. The first six POD modes for 3-hour realizations of the wind at 11.4 m/s are shown in Fig. 36 for the Kaimal model and in Fig. 37 for the Mann model. The colour in the figures represents the POD mode shape ϕ_k in the longitudinal wind direction. The positive or negative values of the POD mode shape only represent relative sense. The black circle represents the outline of the wind turbine rotor. The POD mode shape in the rotor covered range should be considered. It can be observed in the figure that the first POD mode, which is also the most energetic mode, of both the Kaimal model and Mann model wind fields is composed of a main coherent structure. Compared with the Mann model, the main coherent structure of the Kaimal model is more uniformly distributed across the entire rotor plane. However, the contour of the Mann model is relatively smoother. And for higher modes, more patterns that are present
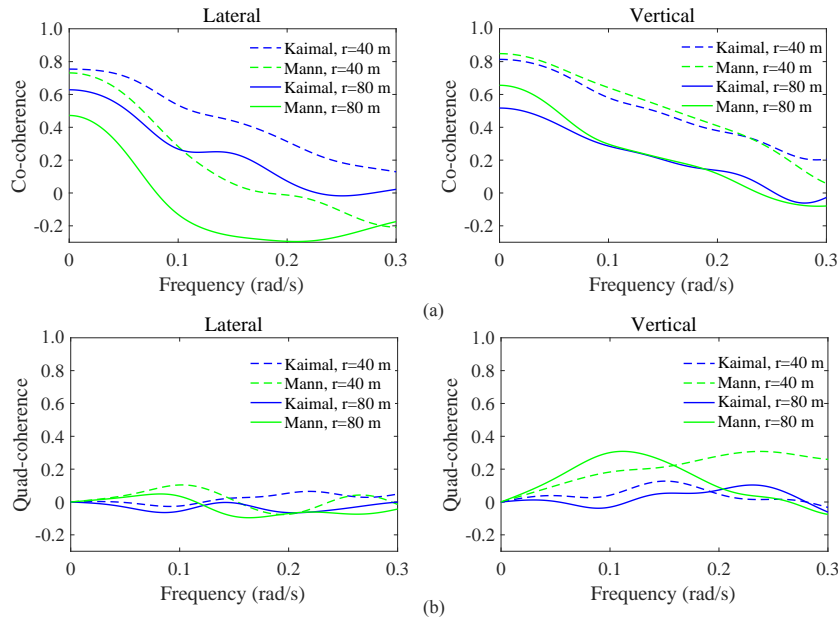
43

Figure 35: (a) Co-coherence and (b) quad-coherence of the wind speed component in the direction of the main wind direction (longitudinal component) at 40 m separation and 80 m separation distance for lateral separation and vertical separation comparing the "Kaimal" and "Mann" wind fields. (Dashed lines denote 40 m separation and solid lines denote 80 m separation.)

as peaks and valleys can be seen, which means that the inhomogeneity of the wind field is more significant. Therefore, the different coherent structures of these two models should influence the dynamic responses of the wind turbine.

To verify the influence of the coherent structure, a completely coherent wind field, whose phase difference between any two points is zero, was used as a reference wind field. However, the turbulence of this wind field still exists in time scale. The "Turb2" wind field described in Section 6.2.2 meets this condition. It has a mean wind speed of 11.4 m/s and turbulence intensity of 14.6%. The wind speed of each point is identical at any time instance, and the time series of every point satisfies the Kaimal spectrum in Eq. (4), so it was used as a reference wind field to compare with the Kaimal wind field and Mann wind field. Fig. 38 shows the power spectra of the blade-root bending moment, tower-top shear force, generated power, and pitch motion under three wind-only conditions with different coherent structures. For the blade-root bending moment and tower-top shear force, one big difference can be seen at the low-frequency range. Although the low-frequency components of the inflow winds are identical among the three wind field models since they follow the same wind spectra, the "Turb2" model sees the largest low-frequency responses, and Mann model shows relatively smaller responses compared with the Kaimal model in Fig. 38. For the uniform but spectral wind field "Turb2", the wind speeds at all points are in phase with each other. If the speed at the reference point (hub center) exceeds 11.4 m/s, then the speeds at all other points are higher than 11.4 m/s. In this circumstance, the variation in the average wind speed seen by the rotor in time-scale is severe due to the lack of a phase lag at different points. Because the average wind speed across the rotor plane deviates more from the rated wind speed, the generated thrust is
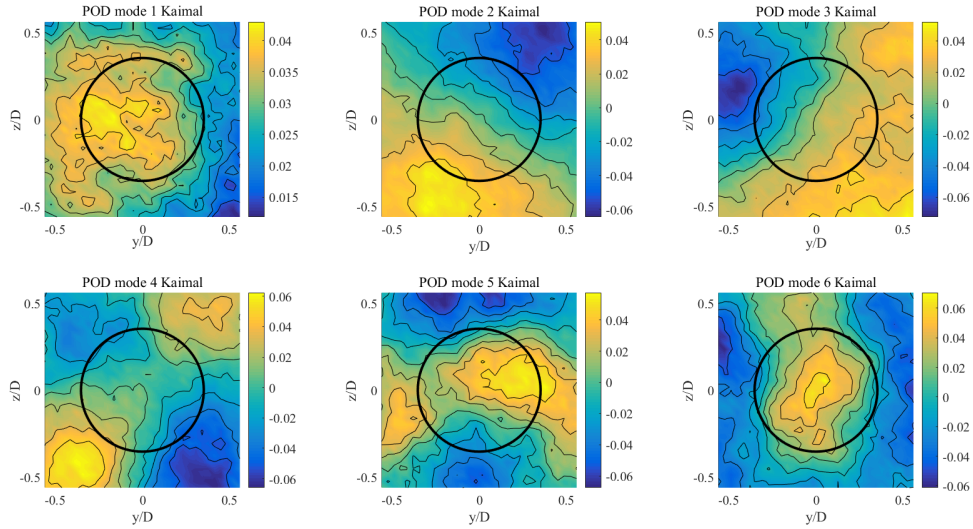
44

Figure 36: First six proper orthogonal decomposition (POD) modes (longitudinal direction, normalized), Kaimal model.
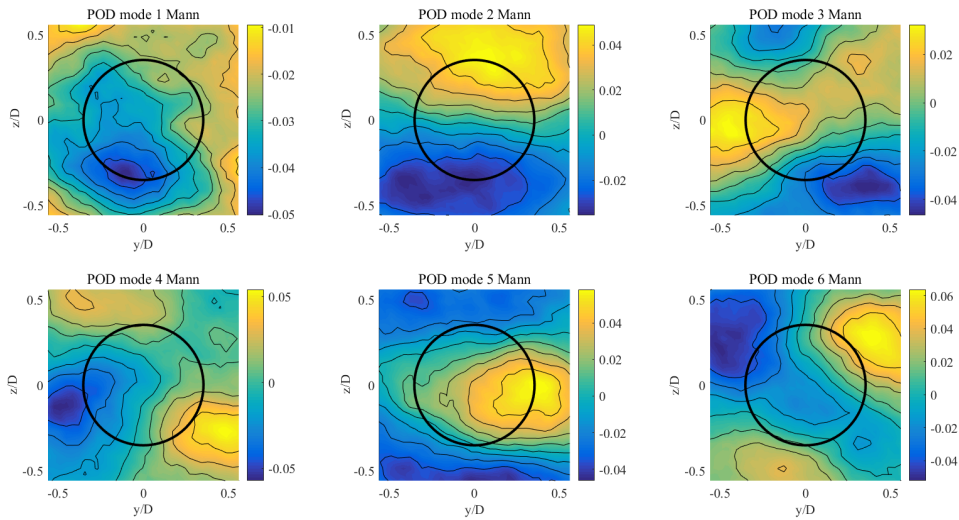

Figure 37: First six proper orthogonal decomposition (POD) modes (longitudinal direction, normalized), Mann model.

expected to decrease significantly and fluctuate severely due to the relationship shown in Fig. 13. Therefore, the mean values of the blade-root bending moment and tower-top shear force under wind field "Turb2" are smallest among the three wind fields as shown in Table 11, while the low-frequency component seen in Fig. 38 is largest for the "Turb2" model. The spectral difference seen at the low-frequency range between the other two models is relatively smaller because they are both partially coherent. Due to the phase difference, the speeds at some points are higher than 11.4 m/s whereas the speeds at other points are lower than 11.4 m/s. The average wind speed of the wind grid is close to 11.4 m/s, though it also varies with time. Apparently, the inflow seen by the rotor is less unsteady in the presence of a coherent structure. It can be seen in Fig. 35 that the Kaimal model shows higher lateral co-coherence values than the Mann model, which represents more correlated wind at lateral separations. The result is that the rotor will be subject to relatively more violent loads under the Kaimal model wind field. This effect on the thrust force directly has an influence on the generated power. Fig. 36 and Fig. 37 also show that the main coherent structure of the Kaimal model is more uniformly distributed across the entire rotor plane compared with the Mann model. The Kaimal model consistently results in more severe low-frequency variation of platform pitch motion. Therefore, in a partially coherent wind field which is more realistic, the generated electric power and the platform pitch motion tend to show fewer fluctuations. The coherent structure also influences the 1P and 3P responses. Large differences at these frequencies are observed in the blade-root bending moment and tower-top shear force. Because the Mann model is the least spatially uniform model among the three wind fields, the blade rotating in this wind field model experiences the most thrust variation, leading to the largest 1P and 3P responses. These responses are obviously smaller under the completely coherent wind field "Turb2".

7. Conclusions

The purpose of this paper is investigating the quality of the wind field generation in model test and their effects on the global responses of 10 MW SPIC floating wind turbine concept by comparing the experimental measurements and numerical simulations. Numerical simulations were performed for the full-scale structure, which were then compared with the upscaled measurements from the model test. A series of wind-only conditions including constant rated wind, below-rated and over-rated wind, over-cut out wind, and rated wind spectra were simulated in both basin model tests and numerical simulations, to calibrate the numerical model parameters and to assess the accuracy of it. In the model test, due to the small variations in the output of each fan and the slight differences among the fans of the wind generation system, the obtained wind speed varies in space and time, and it is not possible to generate an ideal uniform, constant or time-varying wind field. The wind speeds around the hub center were recorded before the formal tests in the basin, and they were input to the numerical simulation to maximize the consistency of external environmental conditions.

Operation mode A, which maintained the rotor speed and blade pitch angle at fixed values corresponding to the mean wind speed, was utilized in the numerical model for comparisons with the experimental tests, to compare the dynamic performances of the wind turbine more clearly. The mean aerodynamic thrusts of the model tests and
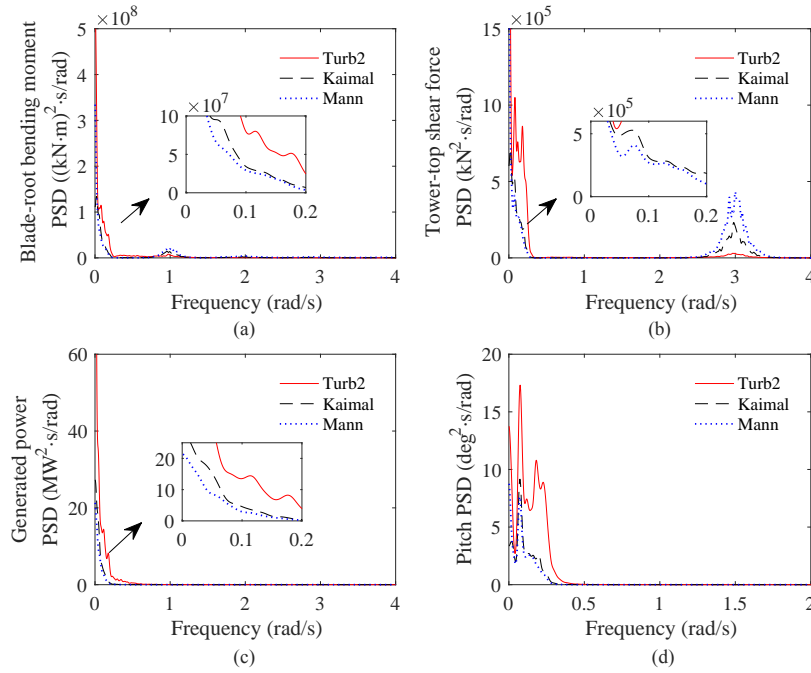
46

Figure 38: Comparisons of power spectra of (a) blade-root bending moment, (b) tower-top shear force, (c) generated power, and (d) pitch motion under three wind-only conditions with different coherent structures.

numerical simulations show agreement under all conditions. However, for rated wind spectra conditions, the numerical results show larger low-frequency responses than the experimental results. The C_t of the full-scale rotor varies more than that of the performance-matched rotor under TSR variation, which means that the aerodynamic thrust in FAST shows a larger spectral peak than that in the model test. Moreover, the wind field in the model test is actually spatially coherent, and the space-scale inhomogeneity indeed reduce the low-frequency component of aerodynamic force. In contrast, the 3P responses are larger when the wind field is less uniform. For over-rated wind speed condition, the 1P responses are obvious. In the model test, if the blade pitch angle of each blade is not totally identical because of the imperfect installation, the responses at 1P can be induced by periodic changes in the moment of rotor thrust, which will not be present in the establishment of the numerical model.

Based on the limitation of the model test, numerical simulations were performed under realistic Operation Mode B to investigate the effects of spatial and temporal variation in the wind field, and to study how different responses such wind fields will cause. The numerical analysis for the dynamic responses and power generation performance of the SPIC concept FWT was conducted in four kinds of rated-speed wind fields, namely, "uniform and constant wind field", "shear and constant wind field", "uniform and spectral wind field", and "turbulent wind field". This can investigate the impact of wind shear, turbulence intensity and coherent structure of the wind fields, and enhance the performance verification of the wind turbine in more complex wind conditions. Operation mode B, with variable rotor speed and blade pitch angles, was used in the numerical analysis, and the natural frequency of the blade pitch controller was tuned

47

to 0.13 rad/s. The wind shear effect on the mean values is limited. When a certain blade experiences a high-speed wind region above the hub height, other blades simultaneously experience a low-speed wind region below the hub height. Since the operation mode is collective blade pitch control, the resultant force generated by the three blades is relatively stable. The effect of wind shear is mainly present at 1P and 3P frequencies. When turbulence intensity increases, the mean values of all mentioned responses decrease. Under turbulent wind conditions, all of the spectra are dominated by the low-frequency component which is induced by the slow variation of wind speed in time-scale. In addition, 3P responses can be seen in the TFx spectra under two turbulent conditions due to the inflow velocity fluctuation during the rotation. The inhomogeneity of a wind field is also caused by spatial coherence, that is, the phase difference between two points in one wind field. This research selected two possible models for generating space-scale turbulent numerical wind fields: 1) the Kaimal spectral and exponential coherence model, and 2) the Mann uniform shear model. The power spectra of wind speed at hub center show that the power concentrated in the low-frequency range is similar between two different wind fields. The co-coherence, quad-coherence and POD modes of the two wind fields were compared to present the coherent structures. Compared with the uniform model and Kaimal model, the Mann model has lower lateral co-coherence, and the main coherent structure of the Mann model is less uniformly distributed across the entire rotor plane. In a partially coherent wind field, which is more realistic, the generated electric energy and the platform pitch motion tend to show fewer fluctuations. However, the partially coherent structure excites great 1P and 3P responses.

Acknowledgement

References

[1] Z. Ren, A. S. Verma, Y. Li, J. J. Teuwen, Z. Jiang, Offshore wind turbine operations and maintenance: A state-of-the-art review, Renewable and Sustainable Energy Reviews 144 (2021) 110886. doi:10.1016/j.rser.2021.110886.

[2] E. Hernandez-Estrada, O. Lastres-Danguillecourt, J. B. Robles-Ocampo, A. Lopez-Lopez, P. Y. Sevilla-Camacho, B. Y. Perez-Sariñana, J. R. Dorrego-Portela, Considerations for the structural analysis and design of wind turbine towers: A review, Renewable and Sustainable Energy Reviews (2020) 110447. doi:10.1016/j.rser.2020.110447.

[3] B. Brussels, Global wind report 2018, Global Wind Energy Council (2019).

[4] W. Shi, H.-c. Park, C.-w. Chung, Y.-c. Kim, Comparison of dynamic response of monopile, tripod and jacket foundation system for a 5 MW wind turbine, in: The Twenty-first International Offshore and Polar Engineering Conference, OnePetro, 2011.

[5] A. Myhr, C. Bjerkseter, A. Ågotnes, T. A. Nygaard, Levelised cost of energy for offshore floating wind turbines in a life cycle perspective, Renewable energy 66 (2014) 714–28. doi:10.1016/j.renene.2014.01.017.

[6] D. Willis, C. Niezrecki, D. Kuchma, E. Hines, S. Arwade, R. Barthelmie, M. DiPaola, P. Drane, C. Hansen, M. Inalpolat, et al., Wind energy research: State-of-the-art and future research directions, Renewable energy 125 (2018) 133–54. doi:10.1016/j.renene.2018.02.049.

[7] Z. Jiang, Installation of offshore wind turbines: A technical review, Renewable and Sustainable Energy Reviews 139 (2021) 110576. URL: https://www.sciencedirect.com/science/article/pii/S1364032120308601. doi:https://doi.org/10.1016/j.rser.2020.110576.

[8] C. Bak, F. Zahle, R. Bitsche, T. Kim, A. Yde, L. C. Henriksen, M. H. Hansen, J. P. A. A. Blasques, M. Gaunaa, A. Natarajan, The DTU 10 MW reference wind turbine, in: Danish Wind Power Research 2013, 2013.

[9] R. He, J. Ji, J. Zhang, W. Peng, Z. Sun, Z. Guo, Dynamic impedances of offshore rock-socketed monopiles, Journal of Marine Science and Engineering 7 (2019) 134. doi:10.3390/jmse7050134.

[10] T. Xu, X. Shi, C. Liu, Y. Wu, S. Liu, X. Fang, J. Liu, S. Qiao, X. Shan, Z. Yao, et al., Stratigraphic framework and evolution of the mid–late quaternary (since marine isotope stage 8) deposits on the outer shelf of the East China Sea, Marine Geology 419 (2020) 106047. doi:10.1016/j.margeo.2019.106047.

[11] L. Zhang, C. Michailides, Y. Wang, W. Shi, Moderate water depth effects on the response of a floating wind turbine, in: Structures, volume 28, Elsevier, 2020, pp. 1435–48. doi:10.1016/j.istruc.2020.09.067.

[12] Y. Liu, S. Li, Q. Yi, D. Chen, Developments in semi-submersible floating foundations supporting wind turbines: A comprehensive review, Renewable and Sustainable Energy Reviews 60 (2016) 433–49. doi:10.1016/j.rser.2016.01.109.

[13] K. Xu, Z. Gao, T. Moan, Effect of hydrodynamic load modelling on the response of floating wind turbines and its mooring system in small water depths, Journal of Physics: Conference Series, IOP Publishing. 1104 (2018) 012006. doi:10.1088/1742-6596/1104/1/012006.

[14] Q. Cao, L. Xiao, X. Guo, M. Liu, Second-order responses of a 10 MW floating wind turbine, considering the full QTF, in: ASME 2019 38th International Conference on Ocean, Offshore and Arctic Engineering, volume 153, American Society of Mechanical Engineers Digital Collection, 2019, pp. 653–68. doi:10.1115/OMAE2019-95661.

[15] Q. Cao, L. Xiao, X. Guo, M. Liu, Second-order responses of a conceptual semi-submersible 10 MW wind turbine using full quadratic transfer functions, Renewable Energy (2020). doi:10.1016/j.renene.2020.02.030.

[16] K. Xu, K. Larsen, Y. Shao, M. Zhang, Z. Gao, T. Moan, Design and comparative analysis of alternative mooring systems for floating wind turbines in shallow water with emphasis on ultimate limit state design, Ocean Engineering 219 (2021) 108377. doi:10.1016/j.oceaneng.2020.108377.

[17] P. Doubrawa, M. J. Churchfield, M. Godvik, S. Sirnivas, Load response of a floating wind turbine to turbulent atmospheric flow, Applied Energy 242 (2019) 1588–99. doi:10.1016/j.apenergy.2019.01.165.

[18] L. Li, Y. Liu, Z. Yuan, Y. Gao, Dynamic and structural performances of offshore floating wind turbines in turbulent wind flow, Ocean Engineering 179 (2019) 92–103. doi:10.1016/j.oceaneng.2019.03.028.

[19] F. Duan, Z. Hu, J. Niedzwecki, Model test investigation of a spar floating wind turbine, Marine Structures 49 (2016) 76–96. doi:10.1016/j.marstruc.2016.05.011.

[20] H. Bredmose, F. Lemmer, M. Borg, A. Pegalajar-Jurado, R. F. Mikkelsen, T. S. Larsen, T. Fjelstrup, W. Yu, A. K. Lomholt, L. Boehm, The triple spar campaign: Model tests of a 10MW floating wind turbine with waves, wind and pitch control, Energy Procedia 137 (2017) 58–76. doi:10.1016/j.egypro.2017.10.334.

[21] F. Madsen, T. Nielsen, T. Kim, H. Bredmose, A. Pegalajar-Jurado, R. Mikkelsen, A. Lomholt, M. Borg, M. Mirzaei, P. Shin, Experimental analysis of the scaled DTU 10MW TLP floating wind turbine with different control strategies, Renewable Energy 155 (2020) 330–46. doi:10.1016/j.renene.2020.03.145.

[22] A. Nybø, F. G. Nielsen, J. Reuder, M. J. Churchfield, M. Godvik, Evaluation of different wind fields for the investigation of the dynamic response of offshore wind turbines, Wind Energy 23 (2020) 1810–30. doi:10.1002/we.2518.

[23] D. S. Dolan, P. W. Lehn, Simulation model of wind turbine 3P torque oscillations due to wind shear and tower shadow, IEEE Transactions on energy conversion 21 (2006) 717–24. doi:10.1109/TEC.2006.874211.

[24] P. Devinant, T. Laverne, J. Hureau, Experimental study of wind-turbine airfoil aerodynamics in high turbulence, Journal of Wind Engineering and Industrial Aerodynamics 90 (2002) 689–707. doi:10.1016/S0167-6105(02)00162-9.

[25] W. D. Lubitz, Impact of ambient turbulence on performance of a small wind turbine, Renewable Energy 61 (2014) 69–73. doi:10.1016/j.

840 `renene.2012.08.015`.

[26] L. P. Chamorro, S.-J. Lee, D. Olsen, C. Milliren, J. Marr, R. Arndt, F. Sotiropoulos, Turbulence effects on a full-scale 2.5 MW horizontal-axis wind turbine under neutrally stratified conditions, Wind Energy 18 (2015) 339–49. doi:`10.1002/we.1700`.

[27] Q. Li, J. Murata, M. Endo, T. Maeda, Y. Kamada, Experimental and numerical investigation of the effect of turbulent inflow on a horizontal axis wind turbine (Part I: Power performance), Energy 113 (2016) 713–22. doi:`10.1016/j.energy.2016.06.138`.

[28] L. Li, Y. Liu, Z. Yuan, Y. Gao, Wind field effect on the power generation and aerodynamic performance of offshore floating wind turbines, Energy 157 (2018) 379–90. doi:`10.1016/j.energy.2018.05.183`.

[29] E. E. Bachynski, L. Eliassen, The effects of coherent structures on the global response of floating offshore wind turbines, Wind Energy 22 (2019) 219–38. doi:`10.1002/we.2280`.

[30] Q. Cao, L. Xiao, Z. Cheng, M. Liu, An experimental study on dynamic behavior of a new concept of 10MW semi-submersible wind turbine, in: The 30th International Ocean and Polar Engineering Conference, OnePetro, 2020.

[31] E. Bachynski, M. Thys, V. Delhaye, Dynamic response of a monopile wind turbine in waves: Experimental uncertainty analysis for validation of numerical tools, Applied Ocean Research 89 (2019) 96–114.

[32] B. Wen, X. Tian, X. Dong, Z. Li, Z. Peng, W. Zhang, K. Wei, Design approaches of performance-scaled rotor for wave basin model tests of floating wind turbines, Renewable Energy (2019). doi:`10.1016/j.renene.2019.10.147`.

[33] B. Jonkman, J. Jonkman, Fast v8.16.00 a-bjj, National Renewable Energy Laboratory.(NREL), Golden, CO (United States) (2016).

[34] Sesam, Sesam hydrod v4. 9, Wave loads & stability analysis of fixed and floating structures. DNV GL (2016).

[35] J. M. Jonkman, G. Hayman, B. Jonkman, R. Damiani, R. Murray, Aerodyn v15 user's guide and theory manual, NREL Draft Report (2015).

[36] M. O. L. Hansen, Aerodynamics of Wind Turbines, 2008.

[37] M. Hall, Moordyn user's guide, Orono, ME: Department of Mechanical Engineering, University of Maine (2015).

[38] IEC, Wind turbine generator systems. Part 1: Safety requirements, Geneva, Switzerland: International Electrotechnical Commission (1999).

[39] IEC, Wind turbine-Part 1: Design requirements, IEC 61400-1, International Electrotechnical Committee: Geneva, Switzerland (2005).

[40] J. C. Kaimal, J. Wyngaard, Y. Izumi, O. Coté, Spectral characteristics of surface-layer turbulence, Quarterly Journal of the Royal Meteorological Society 98 (1972) 563–89.

[41] J. Mann, The spatial structure of neutral atmospheric surface-layer turbulence, Journal of fluid mechanics 273 (1994) 141–68.

[42] B. Jonkman, Turbsim user's guide v2. 00.00, Natl. Renew. Energy Lab (2014).

[43] R. M. Putri, A study of the coherences of turbulent wind on a floating Offshore Wind Turbine, Master's thesis, University of Stavanger, Norway, 2016.

[44] B. H. Jørgensen, J. N. Sørensen, M. Brøns, Low-dimensional modeling of a driven cavity flow with two free parameters, Theoretical and computational fluid dynamics 16 (2003) 299–317.